JOURNAL OF PETROLOGY

Journal of Petrology, 2022, Vol. 63, No. 3, 1–24
https://doi.org/10.1093/petrology/egac012
Advance Access Publication Date: 21 February 2022
Original Manuscript

OXFORD

Neoproterozoic Eclogite-to Granulite-Facies Transition in the Ubendian Belt, Tanzania, and the Timescale of Continental Collision

Isamu Morita[1], Tatsuki Tsujimori[1,2,3], Nelson Boniface[4], Kennet E. Flores[2,3,5], Shogo Aoki[6,7], and Kazumasa Aoki[7]

[1]Department of Earth Science, Tohoku University, Aoba, Sendai 980-8578, Japan [2]Center for Northeast Asia Studies, Tohoku University, Aoba, Sendai 980-8576, Japan [3] Department of Earth and Planetary Sciences, American Museum of Natural History, New York, NY 10024-5192, USA [4]Department of Geology, University of Dar es Salaam, P.O. Box 35052, Dar es Salaam, Tanzania [5]Department of Earth, Marine and Environmental Sciences, University of North Carolina-Chapel Hill, Chapel Hill, NC 27599-3315, USA [6]Graduate School of International Resource Sciences, Akita University, Akita 010-8502, Japan and [7]Center for Fundamental Education, Okayama University of Science, Okayama 700-0005, Japan

*Corresponding author: Telephone: +81-22-795-3614. Fax: +81-22-795-6009. E-mail: tatsukix@tohoku.ac.jp

Received 28 December 2020; Revised 26 January 2022; Accepted 15 February 2022

Abstract

In collision-type orogens, where high-pressure and ultrahigh-pressure (H*P*–UH*P*) metamorphism usually occurs, deeply subducted continental slabs with eclogitized mafic rocks often undergo recrystallization/overprinting with various geothermal gradients after the peak conditions at lower-to-middle-crustal levels. During the crustal stabilization, the transition from eclogite-to granulite-facies is common. We conducted metamorphic petrology and zircon geochronology on (1) bimineralic and (2) partially granulitized eclogites from the Neoproterozoic Ufipa Terrane (Southwestern Tanzania). Microtextural relationships and mineral chemistry define three metamorphic stages: eclogite metamorphism (M1), H*P* granulite-facies overprinting (M2), and amphibolite-facies retrogression (M3). The bimineralic eclogite has a basaltic composition and lacks M2 minerals. In contrast, the kyanite eclogite is characterized by a gabbro-dioritic whole-rock composition and contains inherited magmatic zircon. Although the matrix is highly granulitized, garnet and kyanite contain eclogite-facies mineral inclusions. Phase equilibria modeling revealed *P*–*T* conditions of 2.1–2.6 GPa and 650–860°C for the M1 stage and 1.4–1.6 GPa and 750–940°C for the M2 stage. Zircon with eclogite-facies mineral inclusions from the bimineralic eclogite lacks Eu anomaly in the REE patterns and yielded the M1 eclogite metamorphic age of 588 ± 3 Ma. Zircon overgrowths surrounding the inherited Paleoproterozoic magmatic cores in kyanite eclogite yielded 562 ± 3 Ma. A weak negative Eu anomaly in the REE patterns and the absence of eclogitic mineral inclusions suggest the zircon growths at the M2 H*P* granulite-facies metamorphic stage. These new data indicate an eclogite-to granulite-facies transition time of 26 ± 4 million years (Myr), suggesting a rate of H*P* rock exhumation toward a lower crustal level of 0.7–1.5 mm/year. Furthermore, the density evolution model indicates that buoyant host orthogneiss with low-density gabbro-dioritic eclogite plays an important role in carrying high-density basaltic eclogite. Our 2D thermomechanical modeling also suggests that a slab break-off with a lower angle subduction of <20° triggers the exhumation of the H*P* slab sliver with 20–30 Myr eclogite-to granulite transition time of large H*P*–UH*P* terranes in major collision zones.

Key words: exhumation rate; Pan-African orogeny; Ubendian Belt; Neoproterozoic; kyanite eclogite

INTRODUCTION

The thickening of continental crust is a common geological feature of continental collision zones. This process triggers felsic magma generation due to partial melting of the quartzo-feldspathic lower crust and/or delamination of mafic lower crust via eclogitization, affecting either crustal evolution or stabilization. Classically, continental crust-thickening processes have been studied in both fossilized and on-going collision zones such as the Western Gneiss Region in Norway and the Himalayan–Tibetan orogen in Central Asia (e.g. Walsh & Hacker, 2004; Chung *et al.*, 2009). A widely accepted tectonic scenario for the continental crustal thickening is the magmatic underplating, which enlarges the lower crust (e.g. Ma *et al.*, 1998; Frost *et al.*, 2001; Liu *et al.*, 2008), and occurs in various tectonic settings, including continent–continent collisions. Basaltic magma underplating above the Moho and underplated mafic lower-crustal sections of subducted plates have been seismically identified in several orogens, such as the North Atlantic region and Himalayan–Tibetan orogen (Thybo & Artemieva, 2013; Chen *et al.*, 2015). An alternative tectonic scenario is that the continental thickening could occur by exhuming large H*P*–UH*P* continental slivers after continent–continent collision and subduction. In this scenario, subducted continental slivers rise from greater depths to lower crustal levels, increasing crustal thickness. This process is caused by buoyancy differences between subducted low-density materials and the surrounding rocks (e.g. Ernst *et al.*, 1997; Chemenda *et al.*, 2000; Liou *et al.*, 2009, 2014). The above-mentioned tectonic scenarios satisfactorily explain continental thickening mechanism; however, the timescale of collision-induced crustal thickening remains enigmatic (e.g. Houseman & England, 1993; Mo *et al.*, 2007). Geochronological studies in crustal metamorphic rocks from continent–continent collision zones have shed some light on the timing of geodynamic process (e.g. Song *et al.*, 2006; Mattinson *et al.*, 2006; Liu & Liou, 2011; Kellett *et al.*, 2014; Liao *et al.*, 2016; Butler *et al.*, 2018); however, quantitative petrogeochronological data is critical to elucidate the timescales of the crustal thickening process.

The Neoproterozoic Pan-African orogeny (Fig. 1a) is the most extensive orogenic system preserved on the Earth and triggered the major continental crust formation during the Neoproterozoic era (Grantham *et al.*, 2003; Rino *et al.*, 2008). The Pan-African orogens formed during the continental amalgamation of the Pannotia/Greater Gondwana supercontinents (Rino *et al.*, 2008; Torsvik & Cocks, 2013; Nance & Murphy, 2019). Pan-African orogens are hot: typically characterized by voluminous orthogneiss, migmatite, and granite with some granulites and minor eclogites. Outstanding examples of these units are widely recorded in East Africa (e.g. John *et al.*, 2003; Kusky *et al.*, 2003; Kröner & Stern, 2004; Boniface *et al.*, 2012; Fritz *et al.*, 2013; Boniface & Tsujimori, 2021). Although the most common Neoproterozoic metamorphic rocks in this region are orthogneiss and migmatite (e.g. Ganbat *et al.*, 2021), during the past two decades, local preservations of eclogite and eclogite-facies metamorphic mineral assemblages have been reported within the Mozambique Belt (MZB; Fig. 1b), and its equivalents (e.g. Malawi: Ring *et al.*, 2002; Zambia: John *et al.*, 2003; Tanzania: Boniface & Schenk, 2012).

Exhumed eclogite- and H*P* granulite-facies metamorphic rocks have been formed and preserved in continental collision zones since the Paleoproterozoic era (e.g. Brown & Johnson, 2018; Palin *et al.*, 2020; Tsujimori & Mattinson, 2021). These fundamental metamorphic rocks are key petrotectonic and geochronological indicators to determine the pressure–temperature–time (*P*–*T*–*t*) evolution paths of deep-buried crustal materials and the timing of the underflow. Eclogite-facies assemblages in most H*P*–UH*P* metamorphic terranes have been commonly affected by secondary recrystallization at various geothermal gradients after the peak-pressure conditions. In collision zones, granulite- or upper amphibolite-facies thermal relaxation occurring in the mid-to lower-crustal sections often obliterates the peak eclogite-facies parageneses at various degrees during its exhumation to mid-crustal levels (Carswell & O'Brien, 1993; Faryad *et al.*, 2010). In addition to the metamorphic petrology, some integrated approaches of geochronology and numerical geodynamic modeling on the continental collision zones have provided effective exhumation rates and/or mechanisms (e.g. Warren *et al.*, 2008; Li *et al.*, 2011; Burov *et al.*, 2014; Li, 2014; Sizova *et al.*, 2014). The occurrence of polymetamorphic units containing the eclogite-to granulite transition offers an excellent opportunity to explore the crustal dynamic processes and timescales from continental subduction to subsequent continent–continent collision-induced crustal thickening. The partially granulitized eclogite sequence of the Pan-African Ufipa Terrane in Tanzania (Boniface & Schenk, 2012) represents an exceptional case of study to test the processes mentioned above.

In this study, we present zircon ages of eclogite-facies and granulite overprinting stages in the Ufipa Terrane of the Ubendian Belt (Fig. 1c). We also conducted a metamorphic petrological analysis, including phase equilibria modeling and applied zirconology that involves LA-ICPMS U–Pb dating, trace element geochemistry, and inclusion mineralogy. The combined approach constrained not only the polymetamorphic evolution of the Pan-African eclogite, but also the timing and the timescales of the geodynamic process that control crustal thickening in continental collision zones. We tested our petro-geochronological data against a 2D thermomechanical model. The modeling approach allows a continuous simulation of the crustal thickening process in a cycle from continental subduction/collision to crustal material exhumation. The main focus of the modeling is to test the subduction angle's effect on the exhumation timescale of deeply subducted materials in the common collision zone. The subduction angle is one of the most important factors to be discussed in this paper, as it is strongly suggested to be related to the volume of H*P*–UH*P* terrane, the exhumation timescale, and structural style of H*P*–UH*P* rocks during continental subduction/collision (e.g. Warren *et al.*, 2008; Li *et al.*, 2011; Kylander-Clark *et al.*, 2012; Burov *et al.*, 2014; Li, 2014). Our petro-geochronological dataset supported by 2D thermomechanical modeling provides a better understanding of the timescales of crustal thickening in the continental collision zones and allows to explore the factors of the dynamic exhumation timescale of H*P*–UH*P* materials.

GEOLOGICAL BACKGROUND

The Pan-African orogeny term is widely used to outline an orogenic cycle characterized by a series of tectonic, metamorphic, and magmatic events that led up to the amalgamation of a significant continental domain during the Neoproterozoic era (e.g. Meert, 2003; Veevers, 2003; Kröner & Stern, 2004; Rino *et al.*, 2008). This orogenic cycle culminates with Gondwana's formation, and its rock record is widely distributed in South America, Africa, Arabia, Australia, and Antarctica. In East Africa, the East African Orogen (EAO; Fig. 1a) is synonymous with the Pan-African Orogen (e.g. Stern & Kröner, 1993; Stern, 1994; Fritz *et al.*, 2013). The EAO is a complex unit between East Africa and western Arabia with ~6000 km in length. The belt contains the record of arcs and/or

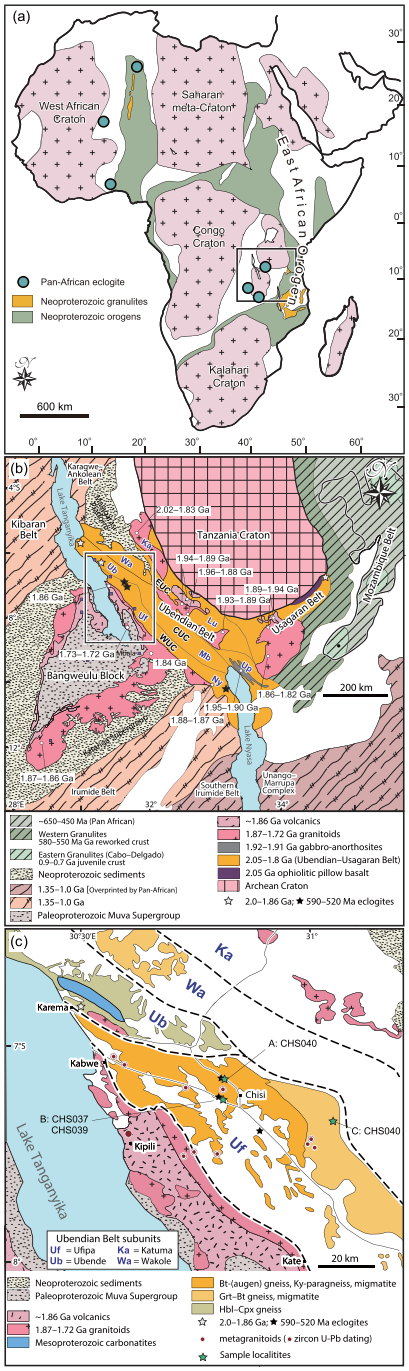

Fig. 1. (a) Geological map of the Precambrian basement and Neoproterozoic reworking area of Africa with illustration of the Pan-African eclogites and granulites area (modified after de Wit & Linol, 2015). (b) Geological map of the central-eastern Africa indicating the Ubendian–Usagaran Belts between the Tanzania Craton and the Bangweulu Block with the magmatic ages in different terranes (modified after Ganbat *et al.*, 2021). Abbreviations for tectonic unit and subunit of the Ubendian Belt are as follows: tectonic unit: Western Ubendian Corridor (WUC), Central Ubendian Corridor (CUC), and Eastern Ubendian Corridor (EUC); and subunit: Ufipa (Uf), Nyika (Ny), Ubende (Ub), Mbozi (Mb), Upangwa (UP), Katuma (Ka), Lupa (Lu), and Wakole (Wa). (c) Local geological map of the northern part of the Ufipa Terrane and the northeastern part of the Bangweulu Block and localities of samples used in this study (modified after Boniface & Tsujimori, 2021; Ganbat *et al.*, 2021).

microcontinents collision against the Archean craton margins. The EAO has a sequence of rocks with an age span of 950–450 Ma (Kröner, 1984). The oldest Pan-African continental collision has been tracked to ~800 Ma, but its major accretionary/collisional cycle is dated as 650–500 Ma (Kröner *et al.*, 1990; da Silva *et al.*, 2005; Rino *et al.*, 2008).

The present-day African continent was in the core of Gondwana supercontinent's and comprised at least four Precambrian cratons (West African, Saharan, Congo (including Tanzania), and Kalahari Cratons (Fig. 1a; Meert & Lieberman, 2008; Itano *et al.*, 2016; Ganbat *et al.*, 2021)). Paleoproterozoic and Neoproterozoic orogenic belts surround these cratons, including the EAO (e.g. Kröner & Stern, 2004; Begg *et al.*, 2009). The Mozambique Belt (MZB) is a major late Neoproterozoic suture zone enclosed in the EAO and hosts juvenile Neoproterozoic rocks that reworked crustal sections of Archean and Paleoproterozoic age (e.g. Boniface & Tsujimori, 2021). Juvenile Neoproterozoic metamorphosed anorthositic and charnockitic rocks within the MZB show emplacement ages between 900 and 700 Ma. This group is locally known as the Eastern Granulite in Tanzania and Cabo-Delgado Nappe Complex in Mozambique (Fig. 1b; Maboko & Nakamura, 1996; Tenczer *et al.*, 2006; Fritz *et al.*, 2013; Viola *et al.*, 2008; Bingen *et al.*, 2009). The reworked Archean-Paleoproterozoic rocks, locally known as the Western Granulite (Fig. 1b), have an age of 580–550 Ma; this age corresponds to the timing of the Neoproterozoic crustal reworking. These reworked rocks define a prominent thrust zone toward the Tanzanian Craton and the Ubendian–Usagaran Belts (Mruma, 1989; Johnson *et al.*, 2003; Cutten *et al.*, 2006; Fritz *et al.*, 2009). Although the Ubedian–Usagaran Belts have been reported to contain rare eclogite associated with the Paleoproterozoic subduction event, the Ubendian subduction event between 1920 and 1860 Ma is slightly younger than that of the 2050–1990 Ma Usagaran Belt (Mruma, 1989; Reddy *et al.*, 2003; Fritz *et al.*, 2005; Boniface & Appel, 2018; Mori *et al.*, 2018; Boniface & Tsujimori, 2019; Tamblyn *et al.*, 2020; Ganbat *et al.*, 2021).

The Ubendian Belt crops out between the Tanzanian Craton and the Bangweulu Block (Ganbat *et al.*, 2021). This tectonic unit displays a poly-orogenic nature and consists of a NW–SE deformed zone of ~150 km width and ~600 km length that extends from eastern Congo to western Tanzania and from northern Malawi to northeast Mozambique (Fig. 1b; Daly, 1988; Lenoir *et al.*, 1994). The Ubendian Belt has classically been considered as a Paleoproterozoic orogenic belt. It is made up of Paleoproterozoic granitoid, migmatite, mafic granulite, rare eclogite, and ultramafic rocks intruded by a few Mesoproterozoic to Mesozoic carbonatites. Some geotectonic units of the Ubendian Belt also recorded Neoproterozoic orogenic events analogous to the MZB (Boniface & Schenk, 2012; Boniface *et al.*, 2014).

The Ubendian Belt consists of eight terranes: Ubende, Wakole, Katuma, Ufipa, Mbozi, Lupa, Upangwa, and Nyika Terranes (Fig. 1b; Daly, 1988; Boniface & Appel, 2018; Ganbat *et al.*, 2021). These terranes formed and evolved through three discrete episodes related to oceanic subduction and collision between the Tanzania, Bangweulu, and Congo Cratons during the Paleoproterozoic (Boniface & Schenk, 2012; Boniface & Tsujimori, 2021; Ganbat *et al.*, 2021). Based on similarities in geology and age distribution, Boniface & Tsujimori (2021) divided the Ubendian Belt into the following three mega-units: Eastern Ubendian Corridor (EUC: Katuma and Lupa Terranes), Central Ubendian Corridor (CUC: Ubende, Mbozi, and Upangwa Terranes), and Western Ubendian Corridor (WUC: Ufipa and Nyika Terranes). The Wakole Terrane does not fit into the above three

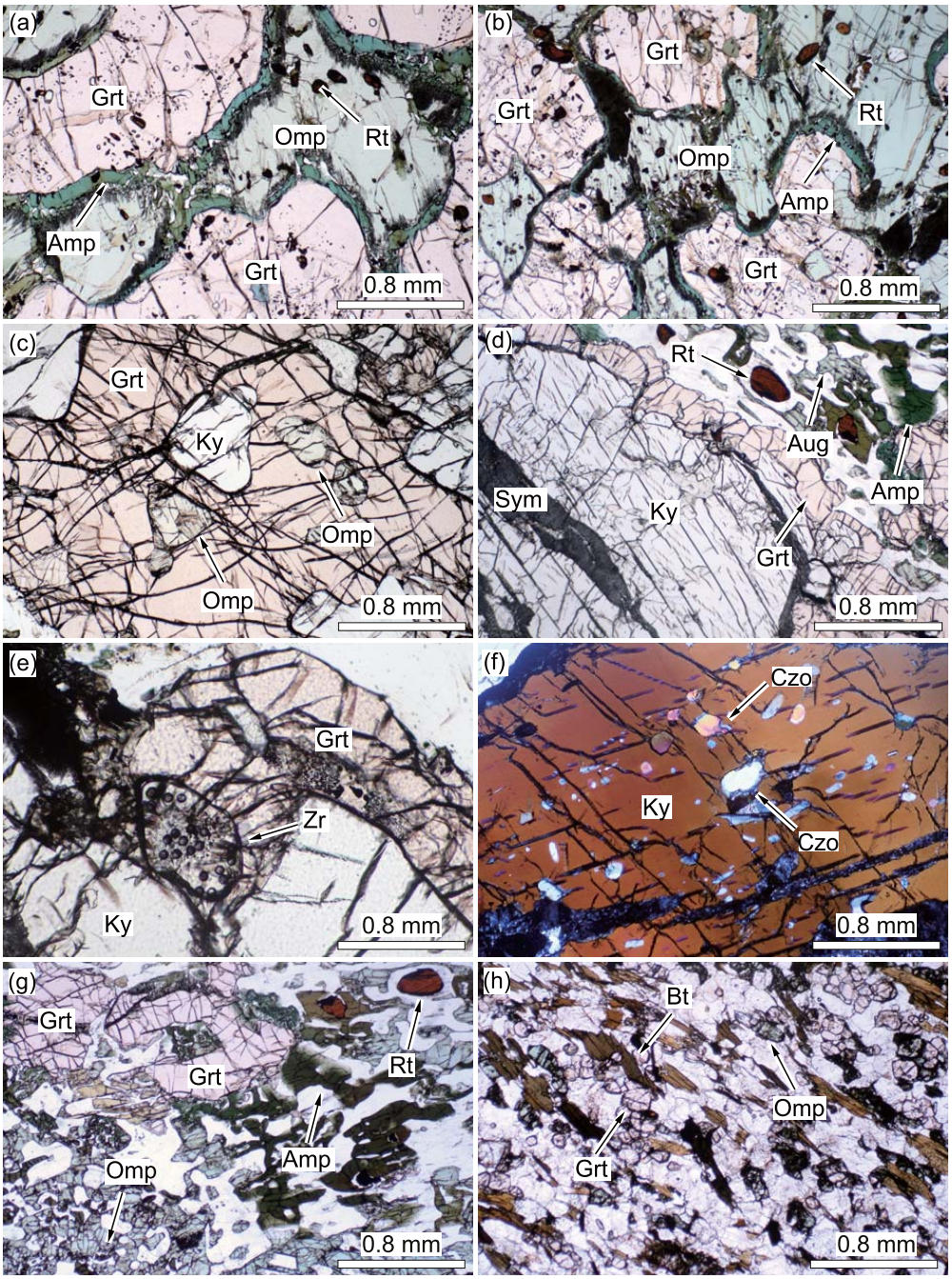

Fig. 2. Photomicrographs showing mineral assemblages in eclogites. (a, b) Bimineralic eclogite (sample CHS040) displaying a secondary clinoamphibole rim developed between garnet and omphacite. (c–g) Granulitized kyanite-bearing-eclogite (sample CHS039) showing (c) omphacite and kyanite inclusions in porphyroblastic garnet, (d) secondary corona garnet around kyanite and symplectite (Sym) textures in kyanite fractures, (e) zircon inclusion in corona garnet, (f) crossed–polarized light view of clinozoisite inclusions in kyanite, and (g) secondary clinoamphibole and Jd-low omphacite in the matrix. (h) Host orthogneiss (sample CHS037) matrix composed of quartz, plagioclase, K-feldspar, mica, and peak assemblage minerals, e.g. garnet and omphacite.

groups because it only consists of Mesoproterozoic metasedimentary rocks without Paleoproterozoic traces.

The EUC is characterized by the predominance of orthogneiss surrounded by metabasite. These rocks are highly deformed and represent a reworked Archean crust of ~2.76 and ~2.55 Ga. The CUC consists of metamorphosed mafic rocks such as amphibolite, hornblende-gneiss, granulite, H*P*-granulite, eclogite lenses (Ubende and Mbozi Terranes), and meta-anorthosite (Upangwa Terrane). The eclogitic rocks record the Paleoploterozoic (1.96–1.89 Ga) subduction zone metamorphism. The WUC encloses the Neoproterozoic (590–500 Ma) eclogite and H*P*-granulite associated with migmatic gneiss. This rock association contains relicts of ~1.99 and ~1.9 Ga arc magmatism and displays shreds of evidence for crustal thickening during Neoproterozoic (Boniface & Tsujimori, 2021).

The Ufipa Terrane eclogite occurs as lenses and lenticular boudins enclosed in semi-pelitic and pelitic gneiss as well as in orthogneiss

(Fig. 1c). Boniface & Schenk (2012) divided the eclogite into bimineralic and kyanite eclogite based on the presence of kyanite in these rocks. The bimineralic eclogite consists of up to 90% of garnet + omphacite with a minor amount of rutile, quartz, apatite, zircon, and secondary clinoamphibole. This type of eclogite displays MORB-like geochemical affinity and was probably formed in the back-arc and/or island-arc tectonic settings. Empirical geobarometry using the albite (Ab) = jadeite (Jd) + quartz (Qz) equilibrium and Zr-in-rutile thermometry studies suggest peak metamorphic conditions at $P > 1.5$–1.7 GPa at $T = 610$–690°C, implying relatively warm subduction with a geothermal gradient of about 11°C/km (Boniface & Schenk, 2012). Metamorphic zircon dating yielded U–Pb ages of 593 ± 20 Ma and 524 ± 12 Ma. Based on the tectonic setting of the bimineralic eclogite and the Neoproterozoic range, these ages are interpreted for the timing of the successive accretions of volcanic-arc rocks derived from the collision with the Bangweulu Block and the Tanzania Craton (Boniface & Schenk, 2012). In contrast, the kyanite-bearing eclogite consists of garnet, omphacite, kyanite, rutile, zoisite, quartz, plagioclase, and zircon. That protolith is a mafic variety of the granite-dominated plutonic complex formed during the Paleoproterozoic. This type of eclogite contains granulite-facies mineral assemblages in the matrix and prograde mineral inclusions of omphacite, rutile, plagioclase, and quartz in garnet porphyroblasts. The average *P–T* method with the THERMOCALC program and other geothermobarometers (e.g. the garnet–plagioclase–aluminosilicate–quartz and the Ab = Jd + Qz barometer) yielded *P–T* condition estimates of 1.6 GPa, 715°C for prograde metamorphism, 2.0 GPa, 785°C for peak eclogite-facies metamorphism, and 1.1 GPa, 700°C for post-eclogite-facies metamorphism (Boniface & Schenk, 2012). Previous zircon U–Pb geochronology yielded ages between ~1.89 and ~1.82 Ga for the protolith and an intercept age of 548 ± 39 Ma for the metamorphic overprint (Boniface & Schenk, 2012). However, it is not clear whether the metamorphic age corresponds to that of the eclogite metamorphism or the H*P* granulite-facies overprint.

MATERIAL AND METHODS

Petrological analyses

The studied main two samples (CHS039 and CHS040) were collected from Site A (7°14′20.34″S 30°59′02.49″E) and Site B (7°08′30.95″S 30°58′47.94″E) of the Ufipa Terrane of the WUC, respectively (Fig. 1c). These two localities lie about 5 km apart within the same coherent terrane. Sample CHS040 is a massive, medium-grained, bimineralic eclogite, which occurs as a ~2m wide unfoliated lens hosted in semi-pelitic, kyanite-bearing garnet–biotite gneiss. Due to the surface weathering of the outcrop, the boundary of the lens was not preserved. In contrast, sample CHS039 is a granulitized coarse-grained kyanite eclogite, occurring as a ~1.5-m-wide block hosted in orthogneiss (sample CHS037). To test the regional extent of eclogite-facies metamorphism, we also collected two bimineralic basaltic eclogites (samples CHS070 and CHS073) from the southern part of the Ufipa Terrane, Site C (7°23′37.02″S 31°17′38.57″E) located about 40 km southeast of Site A and B (Fig. 1c). These samples were geochronologically evaluated to verify the coeval eclogite-facies metamorphism.

We characterize bimineralic eclogite (CHS040) and granulitized kyanite eclogite (CHS039) of the Ufipa Terrane using petrographic rock thin-sections and mineral composition analyses. Microtextures were observed in polished petrographic thin-sections using a JEOL JSM-7001F field emission-scanning electron microscope (FE-SEM), equipped with an Oxford INCA X-act energy dispersive X-ray spectrometers, EDS at Tohoku University. Major-element quantitative analyses were carried out with a JEOL JXA-8230 electron probe microanalyzer at the Okayama University of Science; the analyses were performed with 15 kV accelerating voltage, 12 nA beam current, and 3–5 μm beam size. Natural and synthetic silicates and oxides were used for calibration. The ZAF method (oxide basis) was employed for matrix corrections. Throughout this study, mineral abbreviations are after Whitney & Evans (2010).

Whole-rock major- and trace-element analyses of the two key eclogite samples (CHS039, CHS040) were carried out at Activation Laboratories Ltd. (Canada). The facility uses a Code 4Litho Lithogeochemistry Package; major- and trace-element were determined on lithium metaborate/tetraborate fused homogeneous glass beads using inductively coupled plasma optical emission spectrometry (FUS-ICP-OES) and inductively coupled plasma mass spectroscopy (FUS-ICPMS), respectively. We use the data to constrain the nature of their protolith and to perform the phase equilibria modeling.

We crushed two eclogite samples (CHS039 and CHS040) using a Yasui Kikai Multi Rock Pressure and then sieved them using Nichika Nylon Mesh (#150 [~100 μm] and #100 [~150 μm]) to obtain the proper grain-size for concentrating zircons. Zircon grains were concentrated by combining conventional magnetic and heavy liquid (sodium polytungstate) methods. Hand-picked zircon grains under a binocular microscope were mounted in 1-inch round epoxy resin (Struers Specifix-40) discs and polished to expose their cores. A Metkon Forcipol 1 V grinder and a 3-M aluminum oxide lapping film were used for the polishing. For comparisons, zircons from an orthogneiss (CHS037) hosting a granulitized kyanite eclogite (CHS039) and basaltic eclogites (CHS070 and CHS073) in the southern Ufipa Terrane were also separated for geochronology.

The phase equilibria modeling was performed using THERIAK/DOMINO software (de Capitani & Brown, 1987; de Capitani & Petrakakis, 2010). For the calculation, we used the model system Na_2O–CaO–K_2O–FeO–MgO–Al_2O_3–SiO_2–H_2O–TiO_2 (NCKFMASHT). H_2O was treated as an excess component, and the quartz–fayalite–magnetite (QFM) buffer was considered for the oxidation state. We adopted the thermodynamic dataset of Holland & Powell (1998) and the solid-solution models of minerals used in Tsujimori & Ernst (2014) and shown in Table S1. Whole-rock density was also calculated in the considered pressure–temperature range of 1.0–3.0 GPa, 500–900°C for a total of 10 000 *P–T* points, and these data are visualized with Python in the *P–T* phase equilibria diagram.

Zircon geochronology

Cathodoluminescence (CL) images of zircon in the polished mount of zircon from three sample rocks were observed using a Hitachi S-3400 N SEM, equipped with a Gatan model MiniCL detector at Tohoku University. The CL observation was conducted using a 25 kV accelerating voltage and a 90 nA probe current. Mineral inclusions in mounted zircons are identified using the SEM-EDS and a Horiba LabRam 300 micro Raman spectroscopy at Tohoku University.

Zircon U–Pb and trace element analyses were carried out in the Okayama University of Science using a Thermo Fisher Scientific iCAP-RQ single-collector quadrupole ICP-MS coupled to a Teledyne Cetac Technologies Analyte G2 ArF excimer laser ablation (LA) system equipped with a HelEx 2 volume sample chamber. The LA of zircons was conducted with a laser spot size of 25 μm with a

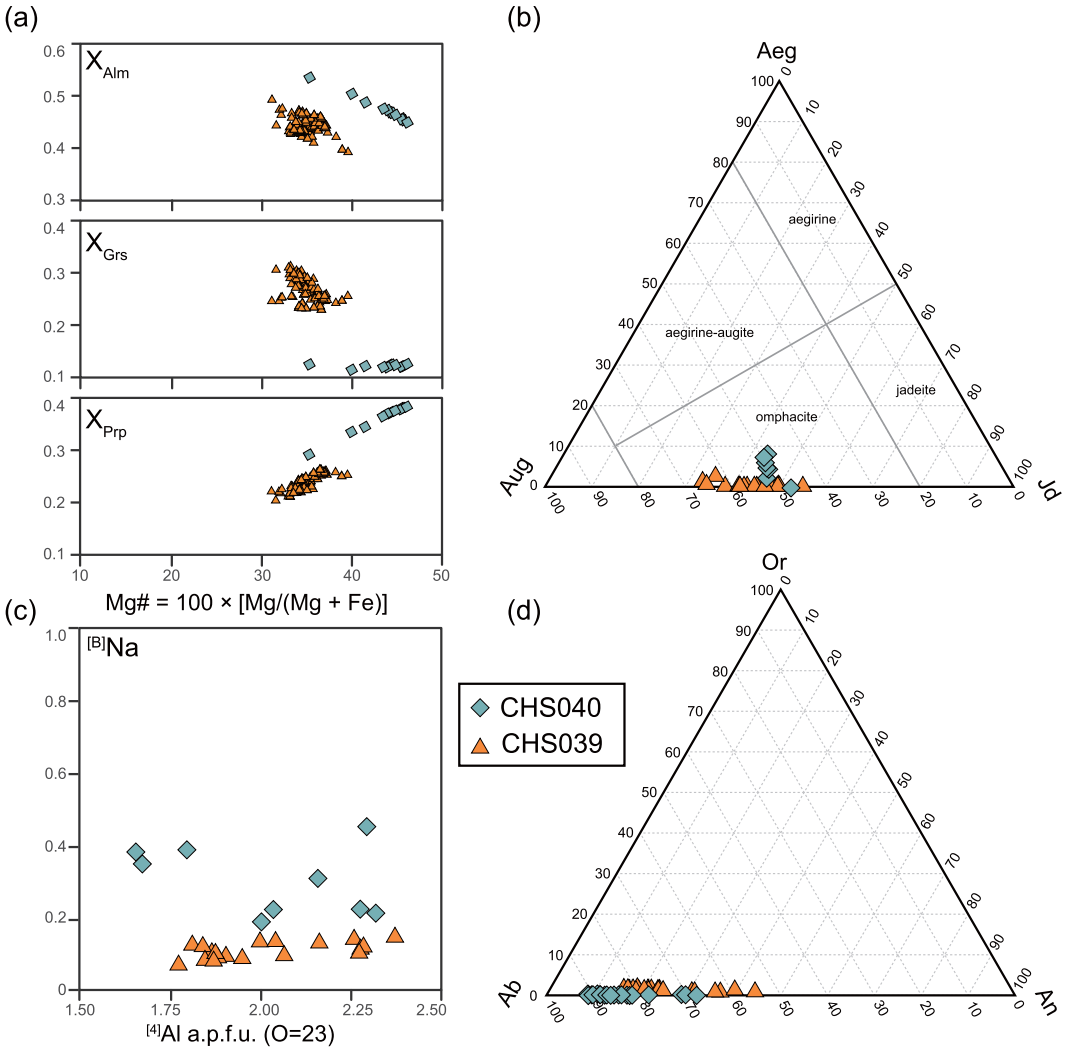

Fig. 3. Compositional trends of garnet, clinopyroxene, clinoamphibole, and plagioclase in bimineralic eclogite (sample CHS040, cyan diamonds) and granulitized kyanite-bearing eclogite (sample CHS039, orange triangles). (a) The Mg# (= 100 × [Mg / (Mg + Fe)]) versus X_{Alm}, X_{Grs}, and X_{Prp} in garnet, (b) aegirine (Aeg)–jadeite (Jd)–augite (Aug) ternary diagram of clinopyroxene, (c) $^{[B]}$Na (Na in the B-site) versus $^{[4]}$Al (Al in tetrahedral site) diagram for clinoamphibole, and (d) anorthite (An)–albite (Ab)–orthoclase (Or) ternary diagram of plagioclase.

fluence of 1.8 J/cm^2 and a repetition rate of 5 Hz. With the ICP-MS, data were acquired on seven isotopes, ^{202}Hg, ^{204}Pb, ^{206}Pb, ^{207}Pb, ^{208}Pb, ^{232}Th, and ^{238}U. ^{202}Hg was monitored to correct the isobaric interference of ^{204}Hg on ^{204}Pb (common Pb). However, corrected ^{204}Pb intensities were too low to calculate U–Pb age for common Pb contamination with a reasonable precision based on ^{204}Pb (Stern, 1997). Therefore, common Pb correction was not carried out in this study. For the analysis, the 91 500 zircon standard (Wiedenbeck *et al.*, 1995, 2004) and NIST SRM 612 glass standard were also analyzed for the correction of ^{206}Pb/^{238}U and ^{207}Pb/^{206}Pb ratios, respectively. As normalization value of 91 500 zircon standard, apparent ^{206}Pb/^{238}U without common Pb correction was used (Sakata *et al.*, 2017; i.e. ^{206}Pb/^{238}U = 0.17928 ± 0.00018). The compiled values of the NIST SRM 612 glass standard by Jochum *et al.* (2011) was used for the correction of the instrumental mass bias of ^{207}Pb/^{206}Pb ratios. The details of analytical method of zircon U–Pb dating are described in Aoki *et al.* (2019, 2020). With the unknown zircons, the Plešovice zircon (Sláma *et al.*, 2008) was analyzed to check the accuracy of the analyses. The weighted mean ^{206}Pb/^{238}U age of 339.52 ± 4.15 Ma and ^{207}Pb/^{235}U age of 340.66 ± 5.33 Ma were obtained (n = 8). Those values were coincident with the reference age of 337.13 ± 0.37 Ma (Sláma *et al.*, 2008). These analyses were mainly conducted for separated and mounted zircons from the samples CHS040, CHS039, and CHS037. In the case of the sample CHS039, we also carried out U–Pb and trace element analyses for zircons on polished petrographic thin-sections. Data plotting and age calculation were performed using IsoplotR (Vermeesch, 2018).

2D thermomechanical modeling

To simulate oceanic and continental plate subduction followed by exhumation, 2D petrological-thermomechanical numerical models are constructed in a size range of 1000 × 300 km. The numerical models are based on the I2VIS code (Gerya & Yuen, 2003) using a conservative finite differences method with a non-diffusive marker-in-cell technique. The models consist of a 201 × 61 nonuniform rectangular grid with a high-resolution area of 300 × 90 km as the investigate subduction channel (Fig. S1a). About 300 000 active Lagrangian

Table 1: Representative EPMA analyses for the Ufipa eclogites

	CHS040				CHS039									
	Grt	Cpx	Amp	Pl	Grt (core)	Grt (corona)	Cpx (inclusion)	Cpx (matrix)	Amp	Pl	Ky	Ms	Bt	Czo
SiO_2	39.70	53.92	44.18	63.88	39.15	39.30	54.30	52.26	38.73	62.94	37.22	45.82	32.27	38.82
TiO_2	0.03	0.23	1.24	0.00	0.14	0.06	0.24	0.32	0.10	0.00	0.04	0.01	1.81	0.25
Al_2O_3	22.58	10.42	14.57	22.73	21.89	22.18	14.06	17.95	18.84	23.22	63.93	34.51	17.92	28.82
Cr_2O_3	0.02	0.09	0.01	0.01	0.03	0.00	0.08	0.02	0.03	0.00	0.10	0.00	0.05	0.00
$Fe_2O_3^T$														6.10
FeO^T	24.06	8.68	0.06	0.44	21.81	23.42	6.10	5.00	0.15	0.13	0.80	2.45	11.16	
MnO	0.54	0.06	8.95	0.00	0.44	0.52	0.03	0.00	14.72	0.02	0.00	0.00	0.00	0.02
MgO	9.97	7.24	14.74	0.00	5.68	6.90	6.49	5.26	10.13	0.00	0.02	0.58	16.00	0.07
CaO	5.12	11.85	9.86	3.68	12.33	9.33	11.83	7.91	10.85	4.42	0.01	0.22	0.28	22.92
Na_2O	0.02	6.33	3.69	9.12	0.03	0.03	6.61	3.64	2.61	8.67	0.00	0.18	0.55	0.02
K_2O	0.00	0.02	0.20	0.02	0.00	0.00	0.00	3.81	0.72	0.19	0.00	10.89	9.54	0.01
Total	102.04	98.83	97.49	99.88	101.49	101.74	99.73	96.16	96.87	99.59	102.12	94.66	94.56	97.01
O=	12.00	6.00	23.00	8.00	12.00	12.00	6.00	6.00	23.00	8.00	5.00	11.00	11.00	13.00
Si	2.97	1.97	6.26	2.82	2.98	2.98	1.94	1.92	5.68	2.79	0.99	3.09	2.75	3.18
Ti	0.00	0.01	0.13	0.00	0.01	0.00	0.01	0.01	0.01	0.00	0.00	0.00	0.10	0.02
Al	1.99	0.45	2.43	1.18	1.96	1.98	0.59	0.78	3.26	1.21	2.00	2.75	1.56	2.78
Cr	0.00	0.00	0.00	0.00	0.00	0.00	0.00	0.00	0.00	0.00	0.00	0.00	0.00	0.00
Fe^{3+}	0.10	0.05	0.75		0.09	0.08	0.00	0.00	1.06					0.42
Fe^{2+}	1.41	0.22	0.31	0.02	1.30	1.40	0.18	0.15	0.75	0.02		0.14	0.69	
Mn	0.03	0.00	0.01	0.00	0.03	0.03	0.00	0.00	0.02	0.00	0.00	0.00	0.00	0.00
Mg	1.11	0.39	3.11	0.00	0.64	0.78	0.35	0.29	2.22	0.00	0.00	0.06	1.76	0.01
Ca	0.41	0.46	1.50	0.17	1.01	0.76	0.45	0.31	1.71	0.21	0.00	0.02	0.02	2.01
Na	0.00	0.45	1.01	0.78	0.00	0.00	0.46	0.26	0.74	0.75	0.00	0.02	0.08	0.00
K	0.00	0.00	0.04	0.00	0.00	0.00	0.00	0.18	0.13	0.01	0.00	0.94	0.90	0.00
Total	8.03	4.00	15.54	4.98	8.03	8.03	3.98	3.90	15.58	4.98	3.01	7.01	7.92	8.42
$^{[B]}Na$			0.15						0.34					
Jd, mol%		39.26					45.21	25.08						
X_{An}				0.22						0.18		0.30		
Mg#	42.49	59.79	82.09		31.70	34.43	65.46	65.22	66.94				71.84	
X_{Alm}	0.49				0.45	0.49								
X_{Grs}	0.13				0.33	0.25								

$Fe_2O_3^T$ = total Fe as Fe_2O_3; FeO^T = total Fe as FeO
Mg# = 100 × [Mg / (Mg + Fe^{2+})] atomic ratio

markers used for the marker-in-cell technique are characterized to trace and mark material scalar properties such as temperature, stress, and strain rate. Numerical equations and details of this approach are based on the previous modeling (e.g. Burg & Gerya, 2005; Gerya *et al.*, 2006; Gerya, 2009; Li *et al.*, 2011; Li, 2014) and shown in supplementary materials. Geochemical and geophysical material properties are based on Turcotte & Schubert (2014), Bittner & Schmeling (1995), Clauser & Huenges (1995), Hofmeister (1999), Poli & Schmidt (2002), Hess (1989), Hirschmann (2000), Johannes (1985), and Ranalli (1995) shown in the supplementary Table S2 and S3. The initial model geometry consists of sticky air/water, granitic upper continental crust, dioritic lower continental crust, basaltic upper oceanic crust, gabbroic lower oceanic crust, lithospheric mantle, and asthenospheric mantle (Fig. S1b). A hydrated mantle fracture zone is prescribed between the oceanic and continental lithosphere as a weak zone to proceed subduction. The model considered free slip boundary conditions at the top, bottom, and side boundaries, erosion and sedimentation process at the surface, melting of rocks, and visco-plastic rheology for each rock unit based on Gerya (2009). Further details of this approach are also described in the supplementary materials.

RESULTS

Petrology

The bimineralic eclogite (sample CHS040, Fig. 2a,b) consists mainly of garnet, omphacite, accessory rutile, apatite, quartz, zircon, and secondary clinoamphibole and plagioclase. Garnet and omphacite made up to ~90% of the sample volume and exhibited granoblastic texture. Both garnet (0.6–0.8 mm in size) and omphacite (0.2–0.6 mm in size) occur as anhedral crystals and contain numerous inclusions of rutile (0.1–0.2 mm in size) and apatite (0.1–0.2 mm in size). Along some of the garnet and omphacite grain boundaries (commonly <0.2 mm in width), a secondary mineral assemblage of dark greenish clinoamphibole and/or symplectite occurs. The symplectite consists of very fine-grained aggregates of clinoamphibole + plagioclase (0.05–0.1 mm in width). Secondary clinoamphibole also appears as patches (0.3–0.6 mm in size) in the matrix. Quartz inclusions occur within garnet, omphacite, and zircon. Although kyanite is not visible in the hand-specimen and thin sections, heavy liquid mineral separation confirmed the presence of fine-grained kyanite (<0.02 mm in size).

The granulitized kyanite eclogite (sample CHS039, Fig. 2c–g) is composed of garnet (~35%), clinopyroxene (~25%), kyanite

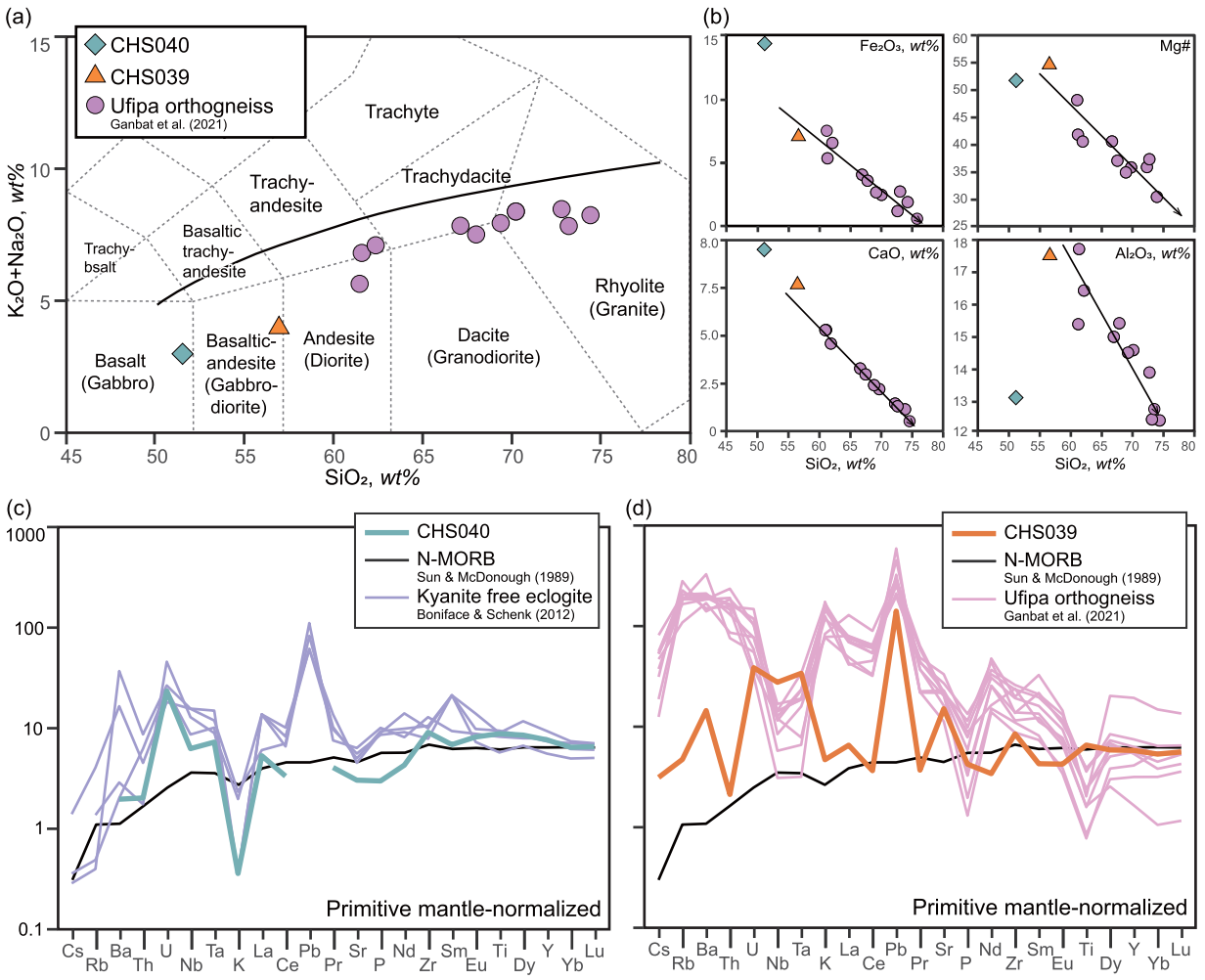

Fig. 4. Whole-rock compositions of the bimineralic eclogite (sample CHS040, cyan diamond) and the granulitized kyanite-bearing eclogite (sample CHS039, orange triangle). For comparisons, orthogneiss (pink circles) in the Ufipa Terrane after Ganbat *et al.* (2021). (a) Total Alkali versus Silica (TAS) geochemical classification diagram for igneous rocks classification, (b) major element variation diagrams of SiO_2 versus Fe_2O_3, CaO, Mg#, and Al_2O_3. (c, d) Primitive mantle-normalized trace element patterns. For comparisons, trace element patterns of N-MORB (Sun & McDonough, 1989), kyanite free eclogite (Boniface & Schenk, 2012), and orthogneiss in the Ufipa Terrane (Ganbat *et al.*, 2021) are also plotted. Normalizing values are from Sun & McDonough (1989).

(~20%), a minor amount (~15%) of rutile, apatite, quartz, zircon, muscovite, relict clinozoisite, and secondary minerals (~5%) represented by plagioclase, clinoamphibole, and biotite. Garnet occurs either as porphyroblasts or as a corona surrounding kyanite. The garnet porphyroblasts (up to 2.0 cm) contain omphacite, kyanite, and rutile (Fig. 2c). The corona occurs as a reaction band (0.1–0.2 mm in width) surrounding kyanite (Fig. 2d), and it coexists with the granulite-facies stage plagioclase in the matrix. It commonly lacks inclusions but is closely associated with rutile and rare zircon (Fig. 2d,e). Kyanite occurs as coarse-grained porphyroblasts up to ~1.2 cm in length and contains inclusions of primary omphacite (0.2–0.4 mm in size), clinozoisite (up to ~0.1 mm in size), and rare muscovite (Fig. 2f). Some kyanite fractures are filled by very fine-grained symplectic aggregates of spinel, plagioclase, and corundum (Fig. 2d). Although the primary omphacite during eclogite-stage is well preserved in both garnet and kyanite, the matrix omphacite is entirely replaced by the intergrowth of jadeite-low omphacite and plagioclase with clinoamphibole (0.05–0.10 mm in width; Fig. 2g).

The host orthogneiss (sample CHS037, Fig. 2h) is composed of quartz (~30%), K-feldspar (~30%), plagioclase (~10%), biotite and muscovite (~20%), and a minor amount (~10%) of garnet, omphacite, kyanite, rutile, apatite, and zircon. Oriented biotite and muscovite (0.4–0.6 mm in width) occur in the lepidoblastic layers. Minor garnet and omphacite (0.1–0.2 mm in size) have well-rounded shapes.

Mineral compositions

Compositional trends for garnet, clinopyroxene, clinoamphibole, and plagioclase of the bimineralic eclogite (sample CHS040) and granulitized kyanite eclogite (sample CHS039) are displayed in Fig. 3; representative analyses are shown in Table 1.

The major element composition of garnet in the bimineralic eclogite is relatively homogeneous and composed of $Prp_{30–39}$ $Alm_{46–54}$ $Grs_{12–13}$ $Sps_{1–2}$ $Adr_{1–2}$ (Fig. 3a). However, gentle compositional zoning from the core to the rim occurs in some porphyroblasts. The compositional variations of garnet porphyroblasts and corona in the kyanite eclogite are $Prp_{21–28}$ $Alm_{42–50}$ $Grs_{25–32}$ $Sps_{1–3}$ $Adr_{0–3}$ and $Prp_{25–28}$ $Alm_{44–48}$ $Grs_{24–27}$ $Sps_{1–2}$ $Adr_{0–2}$, respectively (Fig. 3a). Garnet porphyroblasts in the bimineralic eclogite display a slightly

Table 2: Whole-rock major element (*wt*%) and trace element (μg/g) compositions of the Ufipa eclogites

	CHS039	CHS040
wt%		
SiO_2	56.9	51.49
TiO_2	1.426	1.671
Al_2O_3	17.58	13.13
Fe_2O_3[a]	7.22	14.28
MnO	0.136	0.231
MgO	3.65	6.33
CaO	7.78	9.5
Na_2O	3.95	2.98
K_2O	0.14	0.01
P_2O_5	0.09	0.06
LOI	1.36	0.28
Total	100.23	99.96
μg/g		
Cs	0.1	<0.1
Rb	3	<1
Ba	101	12
Th	0.18	0.15
U	0.81	0.43
Nb	19.7	3.9
Ta	1.39	0.26
La	4.49	3.19
Ce	6.48	5.16
Pb	10	<0.5
Pr	1.02	0.98
Sr	318	56
Nd	4.62	5.07
Zr	95	89
Sm	1.9	2.66
Eu	0.712	1.2
Dy	4.32	5.49
Y	26.4	30.4
Yb	2.63	2.78
Lu	0.415	0.424

Fe_2O_3[a] = total Fe oxides

broader range of Mg# (= 100 × [Mg / (Mg + Fe^{2+})]; 35–46%) than those in kyanite eclogite (31–39%), which increases rimward. The trends of the gentle increases of Mg# and Prp with decreasing of Grs and Alm contents from the core to rim are common in garnet porphyroblasts in both eclogite samples, which show weak retrograde chemical zoning. Mg# in the kyanite eclogite corona garnet around kyanite is relatively homogeneous and has a composition range of 35–40%. The garnet of bimineralic eclogite is relatively enriched in Prp and Alm and depleted on Grs compared to those of the kyanite eclogite.

The compositions of clinopyroxene are plotted in the aegirine (Aeg)–jadeite (Jd)–augite (Aug = diopside [Di] + hedenbergite [Hd]) ternary diagram (Fig. 3b). The Fe^{2+}/Fe^{3+} ratio and end-member components of the clinopyroxene were calculated based on Harlow (1998). Omphacite in the bimineralic eclogite has a composition of $Jd_{42–52}$ $Aug_{48–51}$ $Aeg_{0–9}$, and Mg# ranges from ~63 to 73%. Matrix omphacite coexisting with plagioclase in the kyanite eclogite is characterized by a jadeite-low composition ($Jd_{32–45}$, $Aug_{55–67}$, $Aeg_{0–1}$; Mg# = 67–70%). In contrast, the omphacite inclusions within garnet and kyanite are jadeite-rich, containing up to ~54 mol% jadeite.

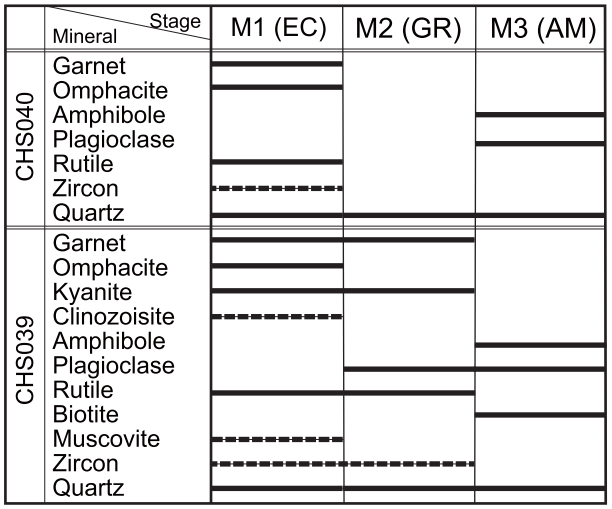

Fig. 5. Mineral parageneses for the different stages of metamorphic recrystallization in bimineralic eclogite (CHS040) and granulitized kyanite eclogite (CHS039).

The structural formulae of clinoamphibole were calculated based on O = 23 and the Fe^{2+}/Fe^{3+} ratio was estimated with total cation = 13, excluding Ca, Na, and K; compositional variations are plotted in $^{[4]}$Al (Al in the tetrahedral site) versus $^{[B]}$Na (Na in the [B]-site) diagram (Fig. 3c). Secondary clinoamphibole in the bimineralic eclogite (CHS040) has a pargasitic composition of 5.7–6.3 Si a.p.f.u, 1.7–2.4 $^{[4]}$Al, 0.2–0.4 $^{[B]}$Na, and 0.7–0.9 $^{[A]}$(Na + K); Mg# varies from ~61 to 84% and Ti reaches up to ~0.15 a.p.f.u. Matrix clinoamphibole coexisting with plagioclase in granulitized kyanite eclogite (CHS039) are also pargasitic and are characterized by 5.6–6.2 Si, 1.8–2.4 $^{[4]}$Al, 0.1–0.2 $^{[B]}$Na, and 0.7–0.8 $^{[A]}$(Na + K). Mg# and maximum Ti content are 59–69% and ~0.19 a.p.f.u, respectively.

Plagioclase compositions are displayed in the anorthite (An)–albite (Ab)– orthoclase (Or) ternary diagram (Fig. 3d). In the bimineralic eclogite, secondary plagioclase occurs along clinoamphibole–omphacite boundaries; the contents vary from 10 to 33 mol%. In the granulitized kyanite eclogite, plagioclases occur in both matrix and fine-grained spinel–plagioclase–corundum symplectic aggregates. The matrix plagioclase has a wide composition range of $An_{16–44}$, and symplectic plagioclase shows wider variations of $An_{10–33}$.

The granulitized eclogite's kyanite contains trace amounts of Cr and Fe as impurities (~0.001 Cr a.p.f.u. and ~0.02 Fe^{2+} a.p.f.u.). The muscovite enclosed in the kyanite is characterized by a composition of ~3.1 Si a.p.f.u. (O = 11) and Na/(Na + K) = 0.02–0.03. Finally, matrix biotite has a composition of Mg# = 70–77% and Ti = ~0.1 a.p.f.u., and clinozoisite inclusions within the kyanite contain 0.4–0.5 Fe^{3+} a.p.f.u.

Whole-rock chemistry

Whole-rock major and trace element compositions for the bimineralic eclogite (sample CHS040) and granulitized kyanite eclogite (sample CHS039) are shown in Table 2. In the Total Alkali versus Silica (TAS) diagram, the bimineralic eclogite displays a basaltic composition, while the granulitized kyanite eclogite plots at the boundary between basaltic andesite and andesite composition (Fig. 4a). Both samples show lower SiO_2 and alkalis than the host Ufipa orthogneiss complex (Ganbat *et al.*, 2021). However, in the major element variations diagrams, the granulitized kyanite eclogite and the Ufipa orthogneiss

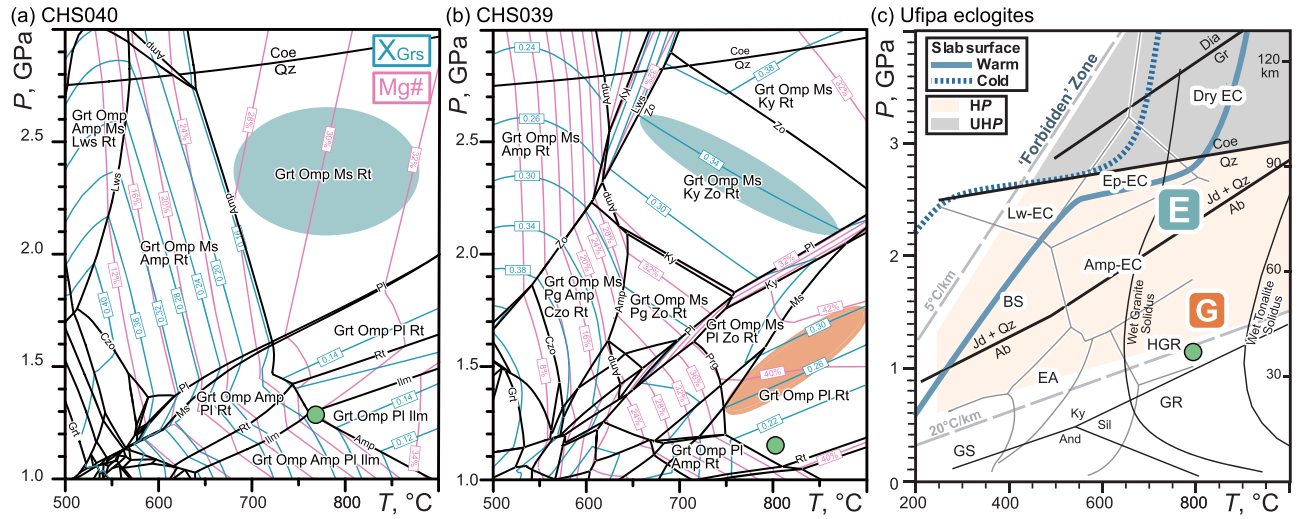

Fig. 6. Phase equilibria diagrams evaluating the stability field of (a) CHS040 and (b) CHS039 eclogites with isopleth of X_{Grs} (blue lines) and Mg# (pink lines) of garnet. Cyan-color and orange-color zones represent the M1 and M2 stage stability fields, and green circle represents maximum *P–T* value of the M3 stage. (c) The estimated *P–T* conditions of the Ufipa eclogites (modified after Liou *et al.*, 2014). Cyan square with initial E represents *P–T* condition of the eclogite-facies metamorphism, orange square with initial G represents that of the H*P* granulite-facies overprinting, and green circle represents maximum *P–T* value of the M3 stage.

are defining common trends negatively correlated with SiO_2 (Fig. 4b). This can be expected from fractional crystallization processes.

The primitive mantle-normalized (McDonough & Sun, 1995) trace element pattern of CHS040 (Fig. 4c) is similar to a previous study by Boniface & Schenk (2012). These patterns are characterized by enriched signatures compared to N-MORB, including significant enrichments in U and Pb, and depletions on K. The signature of CHS039 (Fig. 4d) is also enriched compared to N-MORB, and displays enrichments on Ba, U, Pb, Sr, and Zr. This pattern differs from the trends displayed by the Ufipa orthogneiss, characterized by one order of magnitude enrichments in Rb, Ba, Th, U, and K, and significant depletions on P and Ti.

Metamorphic stages and conditions

Microtextural relationships and mineral chemistry define three metamorphic stages in the Ufipa Terrane eclogite (Fig. 5): eclogite peak metamorphism (M1), H*P* granulite-facies overprinting (M2), and amphibolite-facies retrogression (M3). Note that the bimineralic eclogite lacks M2 minerals. The *P–T* conditions of the M1 and M2 stages were estimated based on the key mineral assemblages, conventional thermobarometry, and phase equilibria modeling.

The whole-rock major element compositions of the two eclogite samples (Table 2) were converted to mole fraction for the phase equilibria model system (NCKFMASHT) with H_2O excess condition. P_2O_5 was removed as apatite and MnO as spessartine components of garnet, which occur in minor amounts relative to the main silicate minerals and other garnet components. The measured total iron oxides as Fe_2O_3 are converted to total Fe mole fraction. In this modeling, the mole fraction of grossular (X_{Grs}) is defined as $X_{Grs} = Ca / (Ca + Fe + Mg)$ because spessartine and andradite components in garnet are neglected in the NCKFMASHT model calculation. Therefore, the calculated X_{Grs} values probably overestimate the measured $X_{Grs} = Ca / (Ca + Fe + Mg + Mn)$ values by up to ~0.03. Uncertainty about the absolute positions of assemblage field boundaries is estimated to be around ±1 kbar and ± 50°C at the 2σ level (Powell & Holland, 2008; Palin *et al.*, 2016).

Eclogite peak metamorphism (M1)

The mineral assemblage of garnet + omphacite + rutile is common to both types of eclogite samples and represents eclogite peak metamorphism. In addition to these minerals, kyanite, clinozoisite, and muscovite also occur as the eclogite peak mineral assemblage in the sample CHS039 (Fig. 5). The phase equilibria modeling for both types of eclogite samples suggests the similar *P–T* space of the M1 stage metamorphism (Fig. 6a,b). With the exception of muscovite in the sample CHS040, the mineral assemblage calculated in this *P–T* space (Fig. 6a,b) correspond to those of the M1 stage (Fig. 5), which is also well explained the occurrence of kyanite in the CHS039. However, the modeling for the sample CHS040 does not strongly constrain the *P–T* conditions because of the broad phase field shown by the mineral assemblage (Fig. 6a). In the case of the sample CHS039, the occurrence of kyanite and zoisite limit the *P–T* space of the M1 stage metamorphism at $P = 1.8–2.8$ GPa and $T = 620–900$°C (Fig. 6b). Although the homogeneous grossular content ($X_{Grs} = 0.12–0.13$) of garnet in the CHS040 is in good agreement with the model, neither gives these strong constraints on the *P–T* conditions (Fig. 6a). The modeled Mg# values (28–32%) of M1 stage garnet are lower than and not consistent with the measured one (35–46%). On the other hand, in the modeling of CHS039, the X_{Grs} (0.30–0.34) and Mg# (>~0.32) isopleth for garnet are in good agreement with analyzed garnet porphyroblasts in the CHS039 (Fig. 6a). Especially, considering the overestimation, the X_{Grs} isopleth of 0.34 value situated in 2.1–2.6 GPa and 650–860°C (cyan-color zone in Fig. 6b) and helps targeting the peak M1 stage condition. The appearance of muscovite and the discrepancy in Mg# of garnet (Fig. 6a) can be attributed to the assumption of H_2O excess and/or the lack of Fe^{2+}/Fe^{3+} estimation, but these assumptions do not significantly compromise the validity of the model.

The Fe^{2+}–Mg distribution coefficient (K_D) between omphacite and adjacent garnet shows a relatively wide range of variations. Comparably low K_D values (CHS040; 2.1, CHS039; ~4.4 on average) suggest relatively high-*T* (872–1054°C) equilibration during the eclogite metamorphism. A summary of the garnet–clinopyroxene

thermometry at 1.5 and 2.0 GPa, applying the calibration of Ellis & Green (1979), Powell (1985), Krogh-Ravna (2000), and Nakamura (2009), is shown in Table 3. In the granulitized kyanite eclogite, this stage is recorded in porphyroblastic garnet and kyanite. The kyanite + clinozoisite assemblage constrains the low-*P* and -*T* limits of the M1 stage by the equilibrium: Ky + Czo = An (in Pl) + Crn + H_2O. The occurrence of kyanite in eclogitic assemblage allows to apply the garnet–clinopyroxene–kyanite–quartz geobarometry; the calibrations suggested by Nakamura & Banno (1997) yield *P* = ~1.9–2.1 GPa at *T* = 925–960°C (Table 3). However, this estimated *P*–*T* condition is in the range of plagioclase and/or out of the clinozoisite stability field, which seems inconsistent with the observed mineral assemblage. This result of geothermobarometry might be caused by the uncertainty of the Fe^{2+}/Fe^{3+} estimation of omphacite and/or incomplete equilibrium of selected garnet and omphacite. The geothermobarometry did not provide further constraints on the *P*–*T* conditions, so based on the phase equilibria model for the sample CHS039 (Fig. 6b), we conclude that it is reasonable the eclogite metamorphism occurred at 2.1–2.6 GPa, 650–860°C (Fig. 6c).

HP granulite-facies overprinting (M2)

The mineral assemblage of corona garnet + Jd-low omphacite + plagioclase in sample CHS039 represents a post-M1 stage of recrystallization. This overprinting is also evidenced by the fine-grained symplectic reaction zones of spinel- and corundum-bearing mineral assemblages. CI-chondrite-normalized REE patterns of omphacite and garnet display HREE depletion compared to those of the M1 stage (Fig. 7). These contrasting signatures on REE might suggest that the corona garnet and the Jd-low omphacite crystalized at a second H*P* event.

The phase equilibria modeling suggests an equilibrium for the M2 mineral assemblage at *P* = 1.1–2.0 GPa and *T* = 750–900°C (Fig. 6b). The mineral assemblage calculated in this *P*–*T* space (Fig. 6b) corresponds to those of the M2 stage (Fig. 5). The corona garnet composition of (X_{Grs}: 0.24–0.27, Mg#: 35–40) is also in good agreement with the model within the range of X_{Grs} overestimation, therefore their calculated isopleths of X_{Grs} (0.26–0.30) and Mg# (36–42%) provided strong constraints on the *P*–*T* conditions of 1.3–1.7 GPa, 750–900°C (orange-color zone in Fig. 6b). On the other hand, the Fe^{2+}–Mg distributions between corona garnet and Jd-low omphacite (K_D values of ~4.3 on average) with plagioclase in the matrix suggest the condition of *P* = 1.4–1.6 GPa at *T* = 895–940°C (Table 3). Despite the instability of the kyanite, *P*–*T* estimation by geothermobarometry is reasonable and consistent with the M2 stage *P*–*T* range constrained by the phase equilibria modeling. The REE chemistry for corona garnet and Jd-low omphacite, geothermobarometry (Table 3) and phase equilibria model (Fig. 6a,b) suggest the M2 granulite-facies overprinting at 1.4–1.6 GPa, 750–940°C (Fig. 6c).

Amphibolite-facies retrogression (M3)

This stage is evidenced by the grain-boundary growth of clinoamphibole in both types of eclogite samples and a secondary-grown clinoamphibole in the granulitized kyanite eclogite. The formation of clinoamphibole during this retrogression stage indicates the infiltration of fluids during decompression. Despite the lack of enough mineral assemblages to define *P*–*T* range, the lower to moderate $^{[B]}$Na content and high $^{[4]}$Al of clinoamphibole are indicative of relatively low-pressure and moderate temperature metamorphism. We also applied the amphibole–plagioclase thermometry and barometry based on the $^{[4]}$Al–Si partitioning calibrated by Holland & Blundy (1994) and Molina *et al.* (2015) for secondary grown amphibole and adjacent plagioclase in each eclogite sample. These geothermobarometers yield *P* = ~1.3 at *T* = ~768°C for the sample CHS040, and *P* = ~1.2 at *T* = ~809°C for the sample CHS039 (Table 3). These results of the *P*–*T* calculations of both eclogite samples are in close agreement with the position of amphibole reaction lines on the phase equilibria diagram (Fig. 6a,b). Taking into account the deficiency of assemblages and the disequilibrium textures of boundary grown clinoamphibole, we interpreted that these *P*–*T* conditions (CHS040; ~1.3 GPa at ~768°C, CHS039; ~1.2 GPa at ~809°C) are maximum values of the M3 amphibolite-facies retrogression stage (Fig. 6).

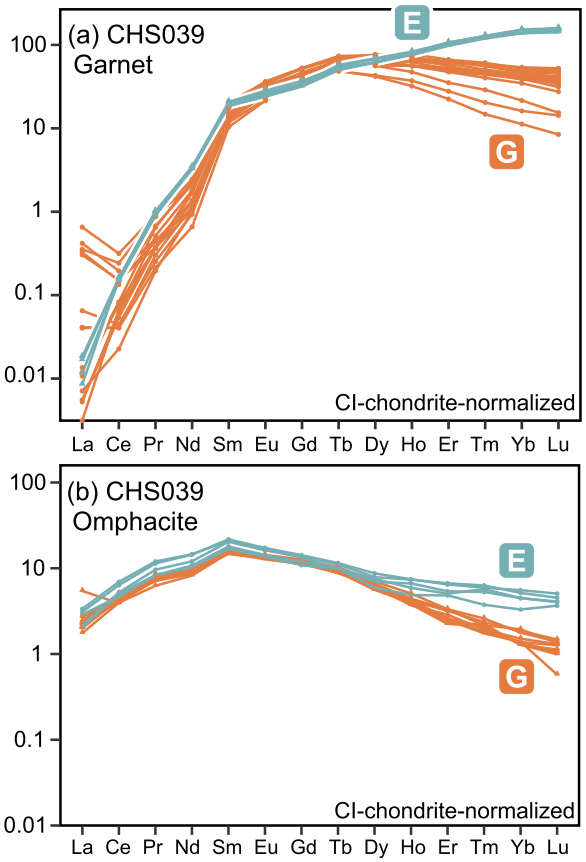

Fig. 7. CI-chondrite normalized REE patterns. (a) REE patterns of porphyroblastic and corona garnets from CHS039, (b) REE patterns of Jd-rich and Jd-low omphacite from CHS039. Normalizing values are from McDonough & Sun (1995). Cyan color and square with initial E represent the prophyroblastic garnet and Jd-rich omphacite during the eclogite-facies metamorphism. In contrast, orange color and square with initial G represent the corona garnet and Jd-low omphacite during the H*P* granulite-facies overprinting.

Zirconology

To constrain the transition time between the peak eclogite metamorphism (M1) and the subsequent H*P* granulite-facies overprinting (M2), we studied the zircons' internal structures and minerals inclusions, and carried out LA-ICPMS U–Pb dating from both types of eclogite samples in Site A and B. For comparison, we also studied zircons from the orthogneiss (CHS037) that hosts the granulitized kyanite eclogite of Site B. Moreover, basaltic eclogites (CHS070 and CHS073) of Site C were also geochronologically evaluated to verify the extent of coeval eclogite-facies metamorphism.

Table 3: A summary of *P–T* estimation of the Ufipa eclogites

Sample	Remarks	Stage	Calibration	*T*, °C	*P*, GPa
Grt–Cpx					
CHS040	Omp^{i}, Grt	M1	Ellis & Green (1979)	978	@1.5
				997	@2.0
			Powell (1985)	965	@1.5
				983	@2.0
			Krogh-Ravna (2000)	936	@1.5
				975	@2.0
			Nakamura (2009)	1025	@1.5
				1054	@2.0
CHS039	Omp^{i}, Grt	M1	Ellis & Green (1979)	940	@1.5
				956	@2.0
			Powell (1985)	928	@1.5
				943	@2.0
			Krogh-Ravna (2000)	882	@1.5
				913	@2.0
			Nakamura (2009)	885	@1.5
				911	@2.0
CHS039	Cpx, Grt^{c}	M2	Ellis & Green (1979)	930	@1.5
				946	@2.0
			Powell (1985)	917	@1.5
				933	@2.0
			Krogh-Ravna (2000)	874	@1.5
				905	@2.0
			Nakamura (2009)	886	@1.5
				912	@2.0
Amp–Pl					
CHS040	Amp, Pl	M3	Molina *et al.* (2015)	611	@0.7
				757	@1.2
CHS039	Amp, Pl	M3	Molina *et al.* (2015)	736	@0.7
				807	@1.2
Grt–Cpx–Ky–Qz					
CHS039	Omp^{i}, Grt	M1	Nakamura & Banno (1997)	@800	2.9
				@850	2.6
	Omp, Grt^{c}	M2	Nakamura & Banno (1997)	@800	2.2
				@850	1.9
Amp–Pl					
CHS040	Amp, Pl	M3	Holland & Blundy (1994)	@700	1.0
				@750	1.2
CHS039	Amp, Pl	M3	Holland & Blundy (1994)	@700	0.8
				@750	1.0

The garnet–clinopyroxene geothermometer apply for both CHS039 and CHS040 eclogites, the garnet–clinopyroxene–kyanite–quartz geobarometer apply for CHS039 eclogite, and the amphibole–plagioclase geothermobarometer apply for both CHS039 and CHS040 eclogites.
Omp^{i} = omphacite inclusion within garnet; Grt^{c} = garnet corona; @ = a given value

Zircon internal texture and mineral inclusions

Zircon grains (100–200 μm) from the bimineralic eclogite (CHS040) are subhedral and vary from elliptical to rounded shape (Fig. 8a). Zircon crystals are characterized by high overall CL, weak internal zoning or sector zoning. SEM-EDS and micro-Raman analyses confirmed relatively large mineral inclusions of quartz, omphacite, garnet, rutile, and apatite (Table 4).

Zircon grains (150–300 μm) within the granulitized kyanite eclogite (CHS039) are euhedral and display prismatic shape with well-rounded terminations (Fig. 8b). Almost all the zircon grains have thick cores exhibiting oscillatory zoning surrounded by thin overgrowth rims. These rims are highly luminescent, and at least two layers are distinguished by CL intensity. They contain a few mineral inclusions; quartz, kyanite, plagioclase, and apatite were identified using EDS and micro-Raman. These identified minerals are included in the oscillatory-zoned cores, and only a few quartz inclusions also occur in the highly luminescent rims (Table 4).

The orthogneiss sample (CHS037) contains euhedral zircon with well-rounded terminations (150–300 μm) and subhedral zircon (100–200 μm), which have rounded and stubby morphology (Fig. 8c). Most zircon grains have thick cores exhibiting oscillatory zoning surrounded by highly luminescent and thin overgrowth rims. These grains contain mineral inclusions of quartz, plagioclase, garnet, kyanite, rutile, and apatite (Table 4).

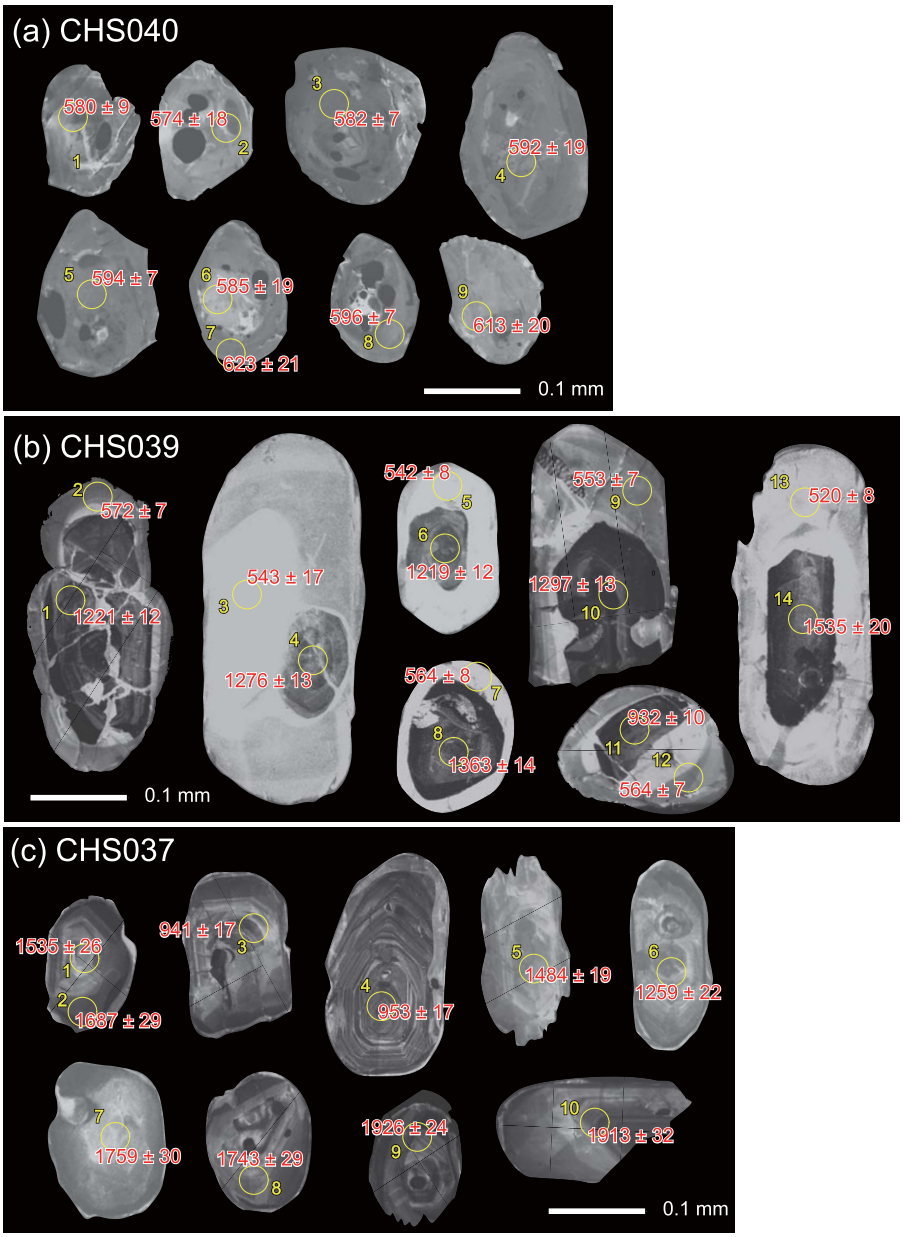

Fig. 8. CL images of analyzed zircon crystals with corresponding ages. The circles indicate the location of the LA-ICPMS analysis. (a) Sample CHS040, (b) Sample CHS039, and (c) Sample CHS037.

Zircon grains (100–250 μm) within the eclogite samples from Site C (CHS070 and CHS073) are subhedral and vary from elliptical to rounded shapes (Fig. S2). Zircon grains mainly have high overall luminescent. Their internal structure is almost characterized by relatively homogeneous or sector zoning texture. However, a few grains have relatively dark homogeneous cores with very thin high luminescence rims. SEM-EDS analyses confirmed mineral inclusions of quartz, rutile, apatite, and clinozoisite.

Zircon U–Pb ages

The LA-ICPMS zircon U–Pb dating results are in Table 5 and Fig. 9. Zircon from the bimineralic eclogite (CHS040) yielded a U–Pb concordant age of 588 ± 3 Ma (Fig. 9a). In contrast, zircon rims and cores from granulitized kyanite eclogite (CHS039) yielded two contrasting ages. The zircon cores spread along a discordia line with an upper intercept age of 1923 ± 19 Ma and a lower intercept age of 560 ± 8 Ma. The overgrowth rims yielded a concordant age at 562 ± 3 Ma (Fig. 9b), which is equivalent to the lower intercept age of the discordia line. We also dated a single-zoned zircon grain (~0.15 mm in size) within a corona garnet in a petrographic thin section (Fig. 2e) from the same sample. This zircon yielded a core age of 1922 ± 74 Ma and a concordant rim age of 566 ± 13 Ma (Fig. 9c). Both ages display large errors but are consistent with the ages yielded by separated zircons. Finally, zircons within the orthogneiss (CHS037) also yielded contrasting intercept ages. Oscillatory cores gave discordant ages with an upper intercept age of 1853 ± 22 Ma and a lower intercept age of 599 ± 55 Ma (Fig. 9d).

The Paleoproterozoic upper intercept ages of the inherited cores of CHS039 and CHS037 zircons represent the timing of magmatic crystallization of their protoliths. These ~1.8–1.9 Ga protolith ages

Table 4: A mineral inclusion assemblage of zircon grains from Ufipa eclogites (CHS040 and CHS039) and host orthogneiss (CHS037)

Sample	Rock type	Zircon size	Remarks	Quartz	Omphacite	Garnet	Rutile	Kyanite	Plagioclase	Apatite
CHS040	Bimineralic eclogite	150–200 μm		+	+	+	+			+
CHS039	Granulitized kyanite eclogite	150–300 μm	core	+				+	+	+
			rim	+						
CHS037	Orthogneiss	150–300 μm				+	+	+	+	+

are plotted within the range of zircon U–Pb age from meta-granitoids from the Bangweulu Block and Ufipa Terrane (e.g. Ganbat *et al.*, 2021), which suggest that sample CHS039, CHS037, and these meta-granitoids have a similar origin.

Zircons of basaltic eclogite from the southern Ufipa Terrane tend to have relatively low U and Pb concentrations through overall this region. Although this feature gives wider errors, zircons from the basaltic eclogites in Site C (CHS070 and CHS073) yielded similar U–Pb concordant ages of 604 ± 19 and 592 ± 36 Ma (Fig. 9e,f). These concordant ages overlap with a timing of the eclogite facies metamorphism recorded in CHS040. The summary of these supporting U–Pb dating results are shown in the supplementary Table S15.

Zircon trace elements geochemistry

The U, Th, and REE trends of zircon crystals are shown in Fig. 10. Zircons from CHS040 have low Th/U ratios (0.003–0.2) with a higher variable spanning range of 2 orders of magnitude (Fig. 10a). Zircons from CHS039 have two different patterns of Th/U ratios. The oscillatory-zoned cores have higher Th/U ratios (0.8–1.0), whereas overgrowth rims have lower Th/U ratios (0.002–0.02). The zircons from sample CHS037 also display similar trends, where the oscillatory zoned core has higher Th/U ratios (0.3–0.8).

Zircon from CHS040 is characterized by flat HREE patterns (Fig. 10b) and shows remarkable positive Ce anomalies ($Ce/Ce* = 95–190$). These patterns indicate that zircon coexisted with garnet (Rubatto, 2002). In contrast, zircon from CHS039 has two different REE patterns (Fig. 10c). The oscillatory-zoned cores have positive steep HREE patterns. They show strong positive Ce anomalies ($Ce/Ce* = 73–300$) and negative Eu anomalies ($Eu/Eu* = 0.3–0.4$). In contrast, highly luminescent rims are characterized by smooth HREE enriched patterns, positive Ce anomalies ($Ce/Ce* = 3–52$), and weak negative Eu anomalies ($Eu/Eu* = 0.3–0.9$). These REE patterns indicate that their zircon rims grew with plagioclase crystallization when garnet began to destabilize during exhumation (Rubatto, 2002; Liao *et al.*, 2016; Štípská *et al.*, 2016).

Phase equilibria and physical modeling

We defined the effective density $\Delta\rho$ as the density difference between the Ufipa Terrane H*P* rocks (bimineralic eclogite, granulitized eclogite, and host orthogneiss) and lithospheric mantle to reveal the buoyancy of subducted rocks. We applied the Preliminary Reference Earth Model (PREM) as the mantle's density profile (Dziewonski & Anderson, 1981). Based on the PREM density evolution (Dziewonski & Anderson, 1981), the density of the mantle is a function of depth, which is represented by $\rho = 2.691 + 0.6924x$ ($x = r/6371$: the normalized Earth radius). Therefore, the PREM density values in the pressure range of 1.0–3.0 GPa decrease from 3.380 to 3.375 g/cm^3 with depth increasing. If the $\Delta\rho$ value is positive, this rock is still in the subduction stage. As the $\Delta\rho$ value goes from 0 to negative, subducted rocks can stagnate and subsequently turn to exhume themselves. The calculated 2D *P–T–*$\Delta\rho$ and 3D *P–T–*ρ diagrams of CHS040, CHS039, and host orthogneiss (Ganbat *et al.*, 2021) are shown in Fig. 11. The black dashed lines in 2D diagrams (Fig. 11a–c) represent the stagnation state with $\Delta\rho = 0$, which is also the depth limit for the exhumation of subducted rocks.

CHS040 has a wide range of positive $\Delta\rho$ values derived from higher density distribution of 3.02–3.57 g/cm^3 (Fig. 11a), and the density change tends to be gentle (Fig. 11d). In the M1 stage *P–T* condition, the current density is ~3.50 g/cm^3, and $\Delta\rho$ is a positive value of ~0.13 g/cm^3. These positive $\Delta\rho$ values derived from high density distribution are controlled by garnet growth (~19.7 mol%) and omphacite (~55.9 mol%) in the M1 stage.

On the other hand, CHS039 has a limited range of positive $\Delta\rho$ values derived from a slightly lower density distribution of 2.89–3.44 g/cm^3 (Fig. 11b) and shows two apparent sharp steps (Fig. 11e). The first step is the result of the kyanite occurrence, and the second step is the result of the quartz-to-coesite transition. In the M1 stage *P–T* condition, the current density is ~3.35 g/cm^3, and $\Delta\rho$ is a negative value of around −0.03. The abundance of garnet (~8.9 mol%) and omphacite (~30.9 mol%) is lower than quartz abundance (~48.9 mol%).

The host orthogneiss shows a lower density range (2.61–3.05 g/cm^3), and the effective density is negative over the entire calculated *P–T* range, although there is a significant increase in density at the quartz/coesite phase boundary (Fig. 11c,f).

Thermomechanical modeling with the 'I2VIS' code

We conducted 2D numerical modeling with the thermo-mechanical code (Gerya & Yuen, 2003) to investigate the subduction angle's effect on the exhumation duration. Figure 12a,b show the calculation results with 20° and 30° subduction angles, and other parameters were assumed to be identical (Table S1). Figure 12c,d show paths tracing the pressure and temperature changes of the markers placed in three different rock units, lower and upper continental and oceanic crust.

Lower-angle subduction of 20° results in a slab break-off at ~41 Myr from the beginning of plate convergence. In this case, large fragments of the oceanic crust remain at the continental crust edge even after the slab break-off (Fig. 12a). The continental crust subducted to a maximum ~120 km depth and exhumed adiabatically to the lower crustal level with a relatively long duration, ~30 Myr.

On the other hand, higher angle subduction of 30° results in a much earlier slab break-off at ~21 Myr. In this case, the slab is broken-off in a shallow section, and most of the oceanic crust is subducted with the edge of the continental crust (Fig. 12b). Despite the deeper subduction, the subducted materials exhume adiabatically to the lower crustal level in a short duration of ~10 Myr (Fig. 12b,d).

Table 5: Representative LA-ICPMS U–Th–Pb analytical data for zircons from the Ufipa eclogites (CHS040 and CHS039) and host orthogneiss (CHS037)

Spot ID.	$^{207}Pb/^{235}U$	2σ	$^{206}Pb/^{238}U$	2σ	$^{207}Pb/^{206}Pb$	2σ	$^{207}Pb/^{235}U$ age	2σ	$^{206}Pb/^{238}U$ age	2σ	$^{207}Pb/^{206}Pb$ age	2σ	U, μg/g	Th, μg/g	Th/U
CHS040															
1	0.76	0.03	0.0943	0.0016	0.0584	0.0018	573.4	15.3	580.6	9.4	544.8	66.9	88.35	1.68	0.152
2	0.78	0.03	0.0932	0.0031	0.0608	0.0018	586.4	19.9	574.2	18.3	633.6	63.5	67.77	13.47	0.199
3	0.724	0.0264	0.0946	0.00115	0.0555	0.0019	553.1	15.6	582.4	6.8	434.1	76.6	61.5	6.89	0.112
4	0.792	0.0375	0.0962	0.00322	0.0597	0.0020	592.1	21.3	592.0	19.0	592.5	72.6	61.7	7.06	0.114
5	0.80	0.03	0.0965	0.0012	0.0603	0.0021	598.0	16.6	594.1	7.0	612.7	74.7	55.08	4.96	0.090
6	0.83	0.04	0.0950	0.0032	0.0632	0.0021	612.0	21.6	584.9	18.7	713.7	70.0	61.61	4.85	0.079
7	0.87	0.06	0.1015	0.0036	0.0625	0.0035	638.0	31.2	623.2	20.9	690.7	118.9	17.13	0.06	0.003
8	0.794	0.0292	0.0969	0.00120	0.0594	0.0021	593.5	16.6	596.4	7.0	582.8	75.3	55.0	5.97	0.109
9	0.80	0.04	0.0997	0.0033	0.0584	0.0018	598.3	20.6	612.9	19.6	543.4	67.7	59.36	5.79	0.097
CHS039															
1	3.113	0.0399	0.2085	0.00228	0.1083	0.0007	1436.0	9.8	1220.9	12.2	1770.8	12.1	263.3	216.51	0.822
2	0.708	0.0263	0.0927	0.00125	0.0553	0.0019	543.4	15.6	571.8	7.4	426.2	77.2	41.0	0.29	0.007
3	0.609	0.1079	0.0879	0.00287	0.0502	0.0087	483.1	68.1	543.3	17.0	206.4	403.8	3.1	0.02	0.007
4	3.096	0.0486	0.2189	0.00247	0.1026	0.0011	1431.6	12.0	1275.9	13.1	1671.4	20.1	97.7	55.55	0.568
5	0.739	0.0375	0.0878	0.00139	0.0611	0.0029	561.9	21.9	542.4	8.2	641.5	103.6	21.3	0.11	0.005
6	2.890	0.0404	0.2081	0.00230	0.1007	0.0009	1379.3	10.5	1218.8	12.3	1637.1	15.8	171.7	81.84	0.476
7	0.763	0.0240	0.0914	0.00142	0.0606	0.0017	575.8	13.8	563.7	8.4	623.7	59.0	62.9	0.56	0.009
8	3.512	0.0574	0.2355	0.00334	0.1081	0.0009	1529.9	12.9	1363.4	17.4	1768.4	14.8	291.8	189.95	0.651
9	0.741	0.0252	0.0896	0.00118	0.0599	0.0019	562.7	14.7	553.1	7.0	601.7	68.0	47.9	0.15	0.003
10	3.290	0.0437	0.2229	0.00245	0.1071	0.0008	1478.7	10.4	1297.2	12.9	1749.9	13.7	196.3	80.95	0.412
11	1.938	0.0344	0.1556	0.00179	0.0903	0.0012	1094.2	11.9	932.4	10.0	1431.8	25.9	98.9	43.15	0.436
12	0.715	0.0242	0.0914	0.00119	0.0567	0.0018	547.4	14.4	563.6	7.0	480.5	69.2	49.5	0.16	0.003
13	0.709	0.0262	0.0839	0.00136	0.0613	0.0020	543.9	15.6	519.1	8.1	649.4	71.5	45.7	0.10	0.002
14	4.006	0.0673	0.2689	0.00383	0.1081	0.0010	1635.5	13.7	1535.1	19.5	1767.1	16.3	182.8	108.81	0.595
In situ															
rim	0.69	0.07	0.0889	0.0032	0.0565	0.0053	534.2	42.00	548.8	19.0	472.2	208.96	8.06	0.22	0.028
*rim	0.88	0.07	0.0941	0.0024	0.0678	0.0044	640.7	39.3	579.5	14.3	862.5	65.4			
*rim	0.80	0.06	0.0943	0.0023	0.0612	0.0035	596.5	32.5	581.0	13.4	646.6	60.4			
*rim	0.77	0.06	0.0936	0.0023	0.0627	0.0037	580.4	33.1	576.9	13.6	698.4	62.3			
*rim	0.80	0.09	0.0920	0.0027	0.0599	0.0053	598.7	51.1	567.3	15.7	598.4	93.7			
CHS037															
1	3.994	0.1109	0.2689	0.00517	0.1077	0.0022	1632.9	22.6	1535.1	26.3	1761.2	36.6	176.3	139.24	0.790
2	4.404	0.1204	0.2992	0.00574	0.1068	0.0021	1713.1	22.6	1687.4	28.5	1744.8	35.7	296.1	124.56	0.421
3	1.879	0.0537	0.1571	0.00303	0.0867	0.0018	1073.8	18.9	940.8	16.9	1354.6	40.6	194.0	116.93	0.603
4	1.952	0.0551	0.1594	0.00307	0.0888	0.0018	1099.1	19.0	953.2	17.1	1400.5	39.5	232.5	136.48	0.587
5	3.84	0.06	0.2588	0.0037	0.1078	0.0009	1602.2	13.4	1483.6	18.9	1761.8	15.7	215.45	85.82	0.788
6	2.962	0.0840	0.2157	0.00417	0.0996	0.0021	1398.0	21.5	1258.9	22.1	1616.9	38.7	142.6	94.88	0.665
7	4.705	0.1308	0.3136	0.00604	0.1088	0.0022	1768.1	23.3	1758.5	29.6	1779.5	36.6	144.8	113.89	0.571
8	4.626	0.1290	0.3105	0.00598	0.1081	0.0022	1754.0	23.3	1743.0	29.4	1767.2	36.8	136.7	83.74	0.613
9	5.513	0.0922	0.3482	0.00497	0.1148	0.0010	1902.7	14.4	1926.0	23.7	1877.3	15.8	141.7	169.76	0.667
10	5.28	0.15	0.3454	0.0066	0.1108	0.0022	1864.8	23.5	1912.7	31.8	1811.9	35.8	178.75	107.76	0.565

In situ data is expressed as analyses of zircon grains included in corona garnet from CHS039.

*rim = T. Tsujimori, unpublished data

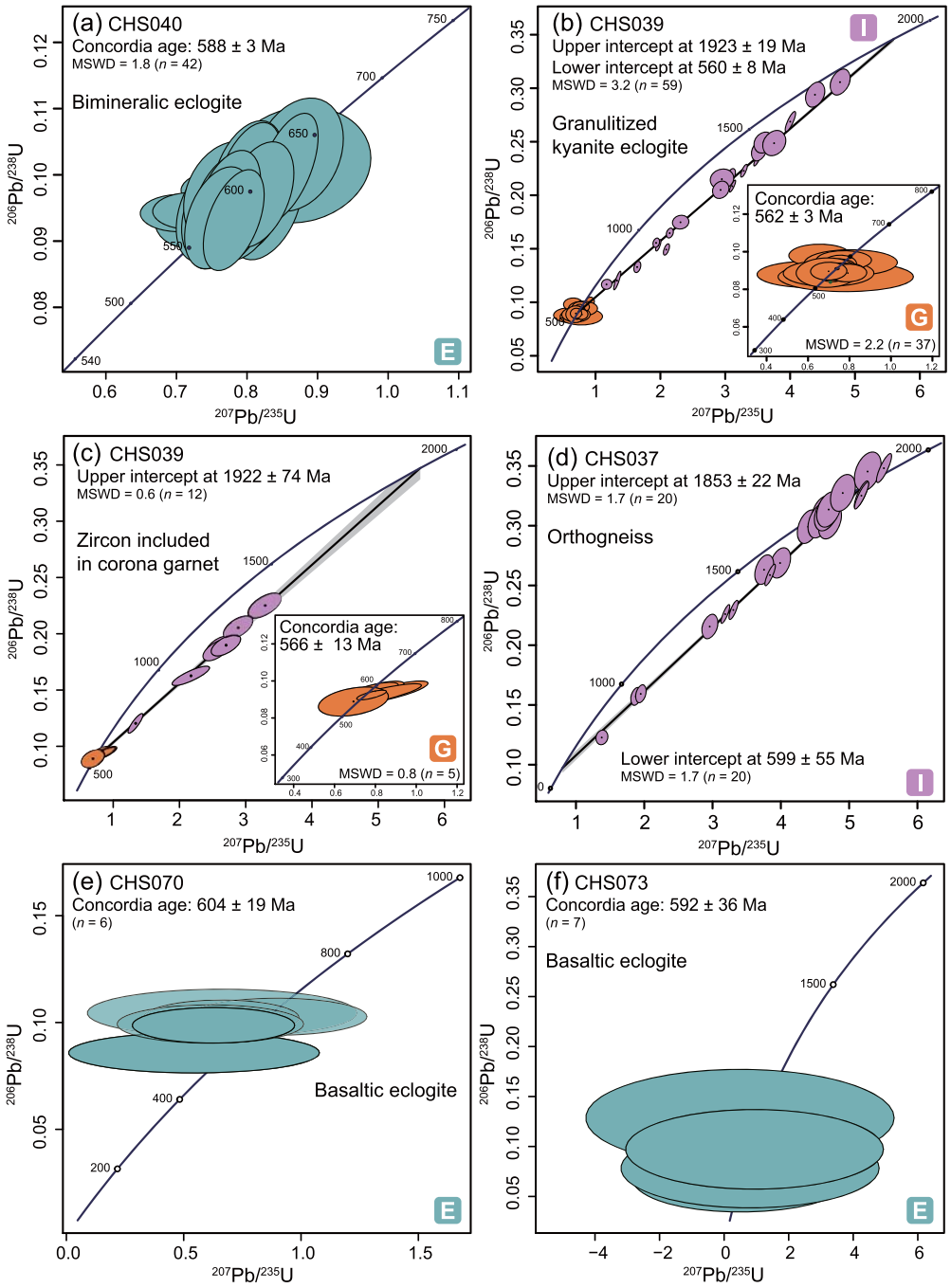

Fig. 9. U–Pb concordia diagrams of dated zircons from the CHS040, CHS039 eclogites, and CHS037 orthogneiss. (a) Concordant age of zircons from bimineralic eclogite (CHS040), (b) upper intercept age of oscillatory zoned cores and concordant age of overgrowth rims of zircons from granulitized kyanite eclogite (CHS039), (c) upper intercept age of cores and concordant age of overgrowth rims of zircon within corona garnet by *in situ* LA-ICPMS dating on thin section, (d) upper and lower intercept ages of zircons from orthogneiss (CHS037), and (e, f) concordant age of zircons from basaltic eclogite (CHS070 and CHS073). Cyan color and square with initial E represent the result from zircons during the eclogite-facies metamorphism; orange color and square with initial G represent the result from zircon rims during the H*P* granulite-facies overprinting; and pink color and square with initial I represent the result from the zircon igneous cores.

DISCUSSION

P–T–t evolution of the Ufipa terrane

The *P–T* geothermobarometries and phase equilibria modeling suggest the transitions from the eclogite peak metamorphism (M1 stage) at 75 ± 7 km depth to the H*P* granulite overprinting (M2 stage) at 48 ± 3 km depth (Fig. 6c). It is not deniable that this decompression path has various possible cooling trends, either heating or isothermal, because of the error of temperature estimations. However, Mg# of the M2 stage corona garnet (35–40%) is slightly higher than the core of the M1 stage garnet porphyroblasts (31–35%) in the sample CHS039. In contrast, K_D values (~4.4) between the M2 stage omphacite and adjacent garnet is slightly lower than the value (~4.3) of the M1 stage. Considering temperature dependence of Mg# of

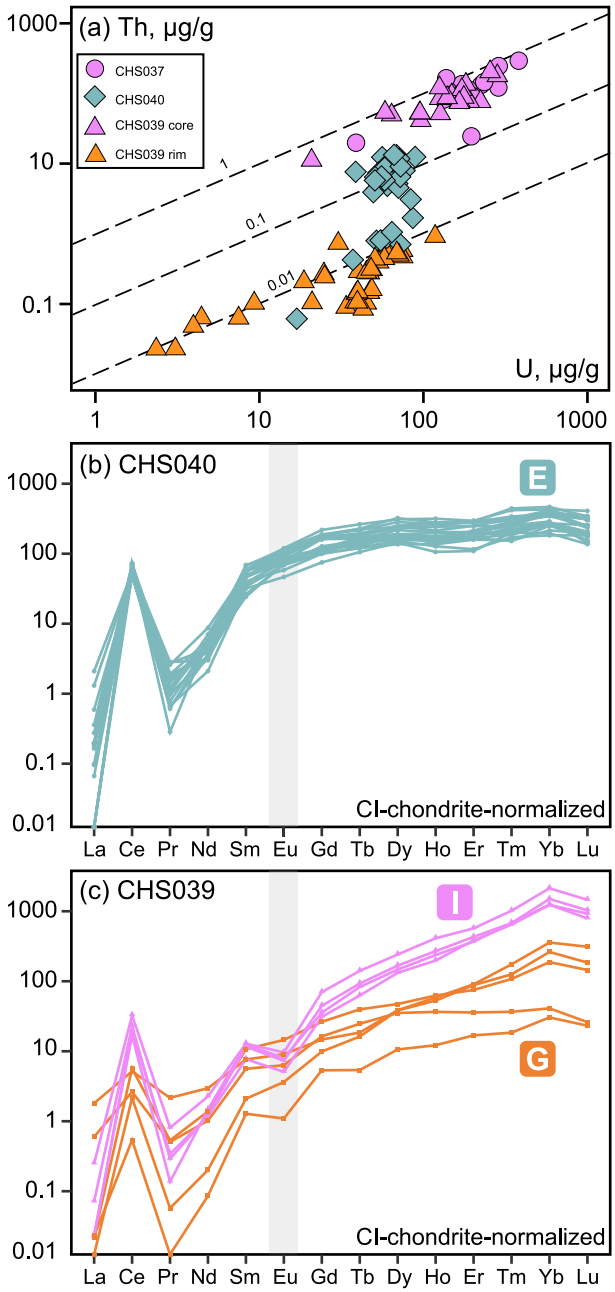

Fig. 10. (a) Typical Th versus U diagram of magmatic and metamorphic zircons. Black dashed lines represent the value of Th/U ratio at 0.01, 0.1, and 1, respectively. (b) REE patterns of metamorphic zircons from CHS040 eclogite, (c) REE patterns of igneous cores, and overgrowth rims of zircons from CHS039 eclogite. Normalizing values are from McDonough & Sun (1995). See Fig. 9 for colors and abbreviations.

garnet and K_D values, these features suggest an almost isothermal or a slight temperature increase during the decompression by the M1 to M2 stage transition. In addition, it is noteworthy that there are abundant symplectic textures in the granulitized kyanite eclogite. The such number of symplectic textures support the nearly isothermal decompression path caused by adiabatic exhumation (e.g. Baldwin *et al.*, 2015). The maximum *P–T* condition of the M3 stage is also consistent with the trend of this decompression path (Fig. 6). Based on these features, we concluded that the transition from the M1 to M2 stage was nearly isothermal decompression despite the estimation error in geothermobarometry and phase equilibria modeling. The previous studies of the Ufipa Terrane H*P* rocks also showed nearly isothermal decompression path in eclogite and gneiss, although the estimated values of *P–T* conditions slightly differed (Boniface & Schenk., 2012; Boniface & Appel., 2018). In fact, such nearly isothermal decompression *P–T* paths are common in other H*P*–UH*P* eclogite of some continental collision zones (e.g. Banno *et al.*, 2000; Baldwin *et al.*, 2004; Hacker *et al.*, 2015; Kellett *et al.*, 2014; Liao *et al.*, 2016; Cao *et al.*, 2019).

The LA-ICPMS zircon U–Pb dating from bimineralic eclogite (CHS040) yielded a concordia age of 588 ± 3 Ma. The dated zircon is homogeneous or displays internal sector zoned texture, and their Th/U ratios are low, which suggests a metamorphic origin (e.g. Yakymchuk *et al.*, 2018). These zircon grains also contain eclogite-facies mineral inclusions (omphacite, garnet, and rutile) and lack of negative Eu anomaly, which indicates that they are coeval with the eclogitic minerals in the matrix (Hermann *et al.*, 2001). Furthermore, the absence of a granulite-facies overprinting in sample CHS040 strongly supports that the zircon formed during the eclogite metamorphism. Therefore, their concordia age of ~588 Ma should represent the M1 stage's timing, the eclogite peak metamorphism.

In contrast, inherited oscillatory-zoned cores with overgrowth rims characterize the zircon from granulitized kyanite eclogite (CHS039). The oscillatory zoning texture in the zircon cores and higher Th/U ratios (0.35–0.82) suggest that they developed during the precursor's magmatic crystallization. Their rims lack oscillatory zoning and display lower Th/U ratios (0.002–0.02) similar to those from H*P* metamorphic zircons (e.g. Flores *et al.*, 2013). The zircon LA-ICPMS dating of the overgrowth rims yielded a concordant age of 562 ± 3 Ma. This age is significantly younger than the age of M1 eclogite-facies zircon in the bimineralic eclogite (CHS040); this younger age was also confirmed by *in situ* ~566 Ma dating in the rim of a zoned-zircon grain within M2 granulite-facies corona garnet on a thin-section of the granulitized kyanite eclogite (CHS039). Considering the lower Zr content of the whole-rock compositions, we could not rule out that these zircon rims were formed by replacement or recrystallization of old inherited cores, not overgrowth. However, negative Eu anomalies and smooth HREE enriched patterns (Fig. 10c) suggest that these rims were formed under the M2 metamorphism condition with plagioclase and corona garnet crystallization when garnet porphyroblasts began to destabilize. Therefore, regardless of their formation process, we think that these zircon rims were formed under the M2 stage conditions, and their younger metamorphic age represents the H*P* granulite-facies overprinting. This is also supported by the absence of omphacite and kyanite inclusions on these zircon rims. Thus, we propose that the concordia age of ~562 Ma represents the M2 metamorphic stage age.

Boniface & Schenk (2012) reported two different U–Pb ages of 593 ± 20 Ma and 524 ± 12 Ma for the timing of collisional metamorphism. The M1 metamorphic age of ~588 Ma is consistent with the eclogite metamorphic age with oceanic closure between the Tanzania Craton and the Bangweulu Block reported by Boniface & Schenk (2012), which is also supported by the continuous age of the basaltic eclogite from the southern part of the Ufipa Terrane. In contrast, the timing of M2 stage metamorphism (~562 Ma) is a new insight into the orogenic evolution. Boniface & Appel (2018) indicate that an oceanic basin closed later in the southern part of the Western Ubendian Corridor (Nyika Terrane), during the collision with the

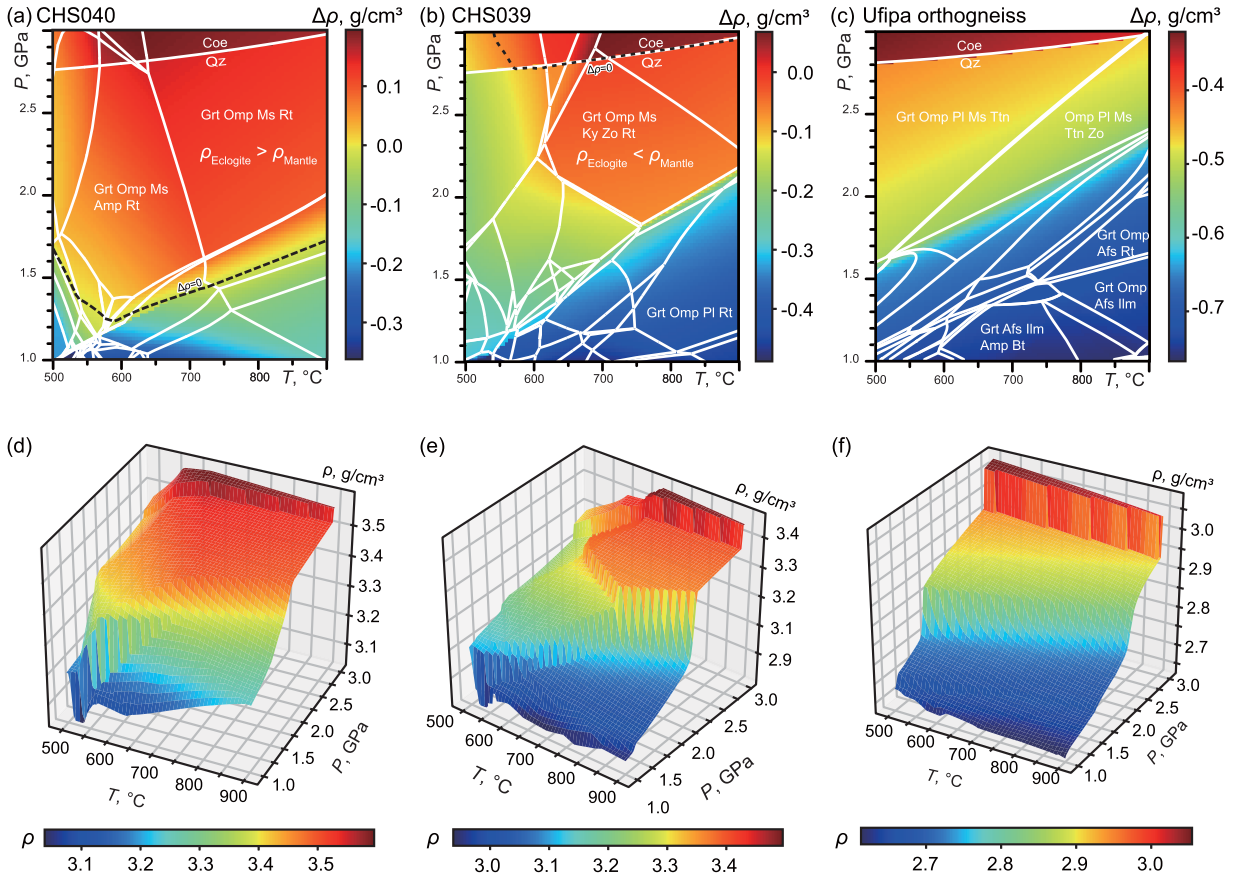

Fig. 11. Two-dimensional effective density distribution on the *P–T* phase equilibria diagrams of (a) CHS040, (b) CHS039, and (c) host orthogneiss in the Ufipa Terrane. Three-dimensional *P–T–ρ* diagrams visualizing density evolution of (d) CHS040, (e) CHS039, and (c) host orthogneiss. The whole-rock dataset of host orthogneiss is based on Ganbat *et al.* (2021).

Bangweulu Block and the Tanzania Craton. This means that the younger age between 530–500 Ma was likely affected by the subduction and closure of different ocean basins. However, younger concordia age of ~524 Ma reported from basaltic eclogite (Boniface & Schenk, 2012) has a wide variation of ages. Due to the lack of trace element geochemistry and mineral inclusion study for zircon, it is also unclear that the resulting age represents the timing of eclogite metamorphism during the collisional event or a later process. Our study revealed the timing of the eclogite metamorphism and the HP granulite overprinting by integrating with zircon U–Pb dating and trace element geochemistry.

Eclogite-to granulite transition caused by buoyancy-driven exhumation

Based on the data discussed above, the transition time Δt between the peak eclogite-facies metamorphism peak (M1 stage) and HP granulite-facies overprinting (M2 stage) in the Ufipa Terrane is estimated as 26 ± 4 Myr. Considering error propagation of the pressure estimation, the Δt and exhumed distance of 29–38 km yield a range of exhumation rate of 0.7–1.5 mm/year. This rate seems relatively slow, but enough to achieve the nearly isothermal decompression path caused by adiabatic exhumation in this region. Much rapid exhumation rates have been reported in some continental collision zones, such as the Dora Maira Massif and/or Kokchetav Massif (Hermann *et al.*, 2001; Rubatto & Hermann, 2001). In common, advection (exhumation) that sufficiently exceeds thermal diffusion's effect caused the adiabatic *P–T* trajectory. This type of exhumation is usually caused by buoyancy differences between the subducted low-density materials and the surrounding mantle rocks (e.g. Ernst *et al.*, 1997; Chemenda *et al.*, 2000; Liou *et al.*, 2014). Warren *et al.* (2008) suggested that this buoyancy-driven exhumation is achieved by the continental crust buoyancy, overcoming subduction-enhancing traction of the oceanic lithosphere. Therefore, the ratio of subduction-enhancing traction to buoyancy may control various exhumation rates and duration of subducted materials in continental collision zones.

The bimineralic eclogite (CHS040) occurred as lenticular boudins with basaltic composition and MORB-like affinity similar to another kyanite-free eclogite, which suggests that these eclogite rocks are derived from the fragments of the oceanic crust. On the other hand, the granulitized kyanite eclogite has higher SiO_2 and alkalis than the bimineralic eclogite. This kyanite eclogite and the Ufipa orthogneiss (Ganbat *et al.*, 2021) display a negative correlation with SiO_2. These suggest that the protolith of the granulitized eclogite is continental derived, a mafic variety of granite-dominant plutonic complex, which is supported by the occurrence of the zircon inherited cores. The occurrence of these oceanic- and continental-derived HP rocks within the Ufipa Terrane indicates the continuous tectonic event, subduction of the oceanic crust followed by continental collision and subduction. These differences of protoliths make the buoyancy structure more complex in the Ufipa Terrane.

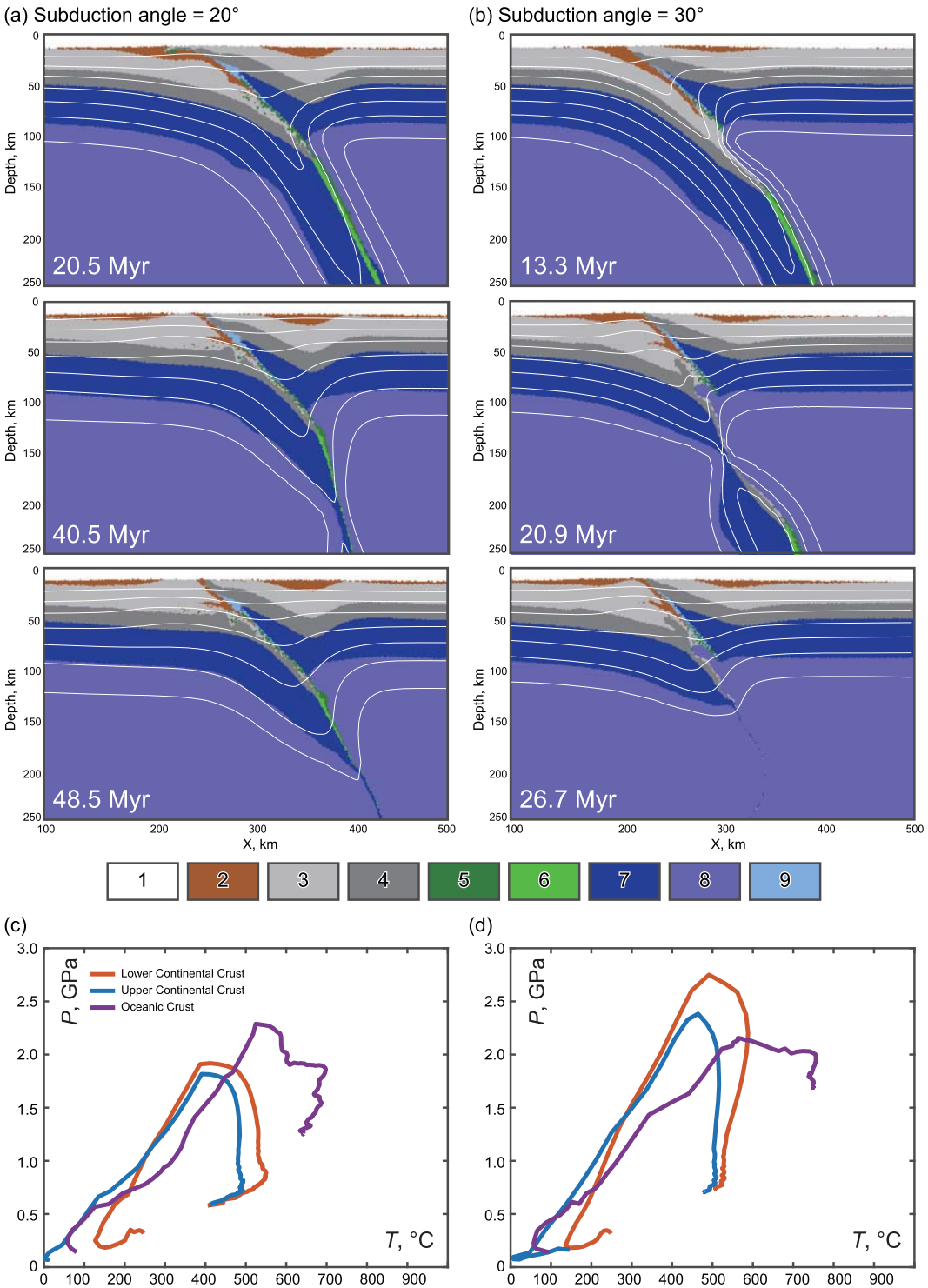

Fig. 12. The evolution models of (a) lower angle (~20°) subduction and (b) higher angle (~30°) subduction are shown by composition and temperature distribution. Colors indicate the rock type as follows: 1-air/water; 2-sediments; 3-upper continental crust; 4-lower continental crust; 5-upper oceanic crust; 6-lower oceanic crust; 7-lithosphere, 8-asthenosphere, and 9-hydrated mantle in the fracture zone. Details of the geochemical and geophysical parameters are shown in Table S2. The *P–T* paths of representative markers on different rock units, in the case of (c) lower and (d) higher angle subduction.

The effective density $\Delta\rho$ is an essential indicator for chasing the state of subduction, stagnation, and exhumation of subducted rocks. Our density distribution profiles show the buoyancy difference in two-types of eclogite samples. In the *P–T* range of the M1 stage, higher density (~3.50 g/cm^3) and positive $\Delta\rho$ value of the bimineralic eclogite suggest that this rock has negative buoyancy, and subduction force is dominant. On the other hand, the granulitized kyanite eclogite shows positive buoyancy and self-exhumation

Table 6: Characteristics of some large-type H*P*–UH*P* terranes in continental collision zones

Locality	Peak H*P*–UH*P* age, Ma	Lower-to-middle crustal age, Ma	H*P*–UH*P* depth, km	Δt, Myr	Reference
Western Gneiss Region	~413	~397	>100	~15	Butler *et al.* (2018)
Eastern Himalaya	~38	15–13	60–70	~25	Kellett *et al.* (2014)
Ufipa	~588	~562	~80	~26	This study
Dabie-Sulu	235–225	215–208	>100	10–27	Liu & Liou (2011)
Qaidam	~423	~403	>100	~20	Song *et al.* (2006)
North Qinling	~497	476–447	> ~60	21–50	Liao *et al.* (2016)

The eclogite-to granulite (and/or amphibolite) time gap (Δt) is compared in different era.

ability supported by lower density (~3.35 g/cm^3) and negative $\Delta\rho$ value in the M1 stage. These results are caused by a difference in protolith composition of the two types of eclogite samples (i.e., basaltic or gabbro-dioritic). Basaltic eclogite has a wide range of high-density zone derived from a high abundance of garnet and omphacite. A lower density distribution of gabbro-dioritic eclogite is resulted from higher quartz abundance than garnet and omphacite. Therefore, there is a significant increase in density at the quartz/coesite phase boundary. Note that the presence of host pelitic gneiss and/or orthogneiss is another critical factor for high-density rock transportation. The effective density across the subduction channel depends on the volumetric ratio of eclogite and low-density materials, and it controls the exhumation rate (Wang *et al.*, 2019). The rapid decline in the transport capacity of felsic rocks at the quartz/coesite phase boundary is consistent because no UH*P* rocks have been identified in the Ufipa Terrane and are limited in other continental collision zones. However, these host rocks in the Ufipa Terrane remain positive buoyant even though the UH*P* phase. Although the difficulty of constraining the volumetric ratio of materials in the subduction channel precludes a quantitative discussion, the presence of these host rocks, which remain positively buoyant even in the UH*P* condition, was confirmed to be a factor in efficiently transporting the high-density eclogite.

Geodynamic timescale in continental collision zone

How does the timescale of eclogite-to granulite transition in the Ufipa Terrane differ from other continental collision zones? Kylander-Clark *et al.* (2012) suggested that the exhumation duration estimated from eclogite-to granulite transition time was associated with the size of the H*P*-UH*P* terrane. Large-type orogenic terranes such as the Western Gneiss Region, Qaidam, and Dabie-Sulu (>20 000 km^2) reported relatively longer exhumation duration (>15 Myr) than small-type (<10 000 km^2) orogenic terranes such as the Dora Maira Massif or Kokchetav Massif (<10 Myr). It is noteworthy that the Neoproterozoic H*P* terranes of the Ubendian Belt (Tanzania), Ufipa, and Nyika Terranes (~16 000 km^2) are one of the exceptional large-type orogenic terranes. Table 6 shows some examples of eclogite-to granulite transition time from the Western Gneiss Region, Eastern Himalaya, Dabie-Sulu, Qaidam, and North Qinling (Song *et al.*, 2006; Mattinson *et al.*, 2006; Liu & Liou., 2011; Kellett *et al.*, 2014; Liao *et al.*, 2016; Butler *et al.*, 2018). Compared to the Δt in other continental collision zones in both Paleozoic and Cenozoic, the values overlap within the similar range of ~20–30 Myr regardless of each collisional event's age. The Δt of ~20–30 Myr might be a geodynamic function of lower crustal stabilization followed by a single continental collision event.

The value of Δt is primarily affected by the ratio of subduction-enhancing traction and buoyancy of continental slab. The volume of H*P*–UH*P* terrane is one of the factors determining this ratio (Warren *et al.*, 2008; Kylander-Clark *et al.*, 2012; Burov *et al.*, 2014). Large orogenic terranes are characterized by lower angle subduction, where need duration to weaken the entire lithosphere due to their large volume. Therefore, it takes a longer time for buoyancy to overcome traction (Warren *et al.*, 2008). Besides, as the subduction angle is lower, the exhumation rate's vertical component is limited in case the H*P*–UH*P* domain exhume follows the same trajectory as subduction (Kylander-Clark *et al.*, 2012). Hence, at least the Δt of 20–30 Myr is required to exhume large volume H*P*–UH*P* terranes from greater depth to lower crustal levels in continental collision zones.

Our 2D thermomechanical modeling revealed the effect of a slight change in subduction angle of 10° to the timing of the slab break-off and exhumation duration of subducted rocks (Fig. 12). Lower angle (~20°) subduction characteristic of large-type orogenic terranes induced deeper level slab break-off. In this case, the continental crust buoyancy is suppressed by leaving large fragments of the oceanic crust even after the slab break-off, which increases the exhumation duration. On the other hand, in a small-type orogenic case where the subduction angle is higher (~30°), the continental crust buoyancy predominates, as most of the oceanic crust are broken-off, hence the exhumation to the lower crustal level is achieved in a short duration. However, various other parameters besides the subduction angle may be involved, such as the abundance of sediments and/or continental materials, the convergence rates, and the crustal strengths controlled by the thermo-rheological structure (Warren *et al.*, 2008; Burov *et al.*, 2014; Wang *et al.*, 2019). Although these parameters are highly controversial and should be tested through complete regional modeling with reproducing burial and exhumation paths of H*P*–UH*P* rocks (Burov *et al.*, 2014), the subduction angle is one of the most important factors that primary controlled the exhumation and structural style of H*P*–UH*P* rocks during continental subduction/collision (e.g. Li *et al.*, 2011; Li, 2014).

During the exhumation from the eclogite-facies depth, subducted continental crust can be underplated to the hanging wall continental crust (Fig. 13a,b). This process promotes the crustal thickening and, subsequently, the exhumed and/or underplated slab recrystallizes in a lower portion of the thickened crust. In this scenario, the timing of an H*P* granulite-facies overprinting (~562 Ma) of the Ufipa Terrane can rephrase the timing of lower crustal stabilization. Assuming 30–35 km for a crustal thickness of the hanging-wall crust before the collision, our new data suggest up to ~40% increase of crustal thickness due to the collision. More importantly, this type of crustal thickening process can require 20–30 Myr.

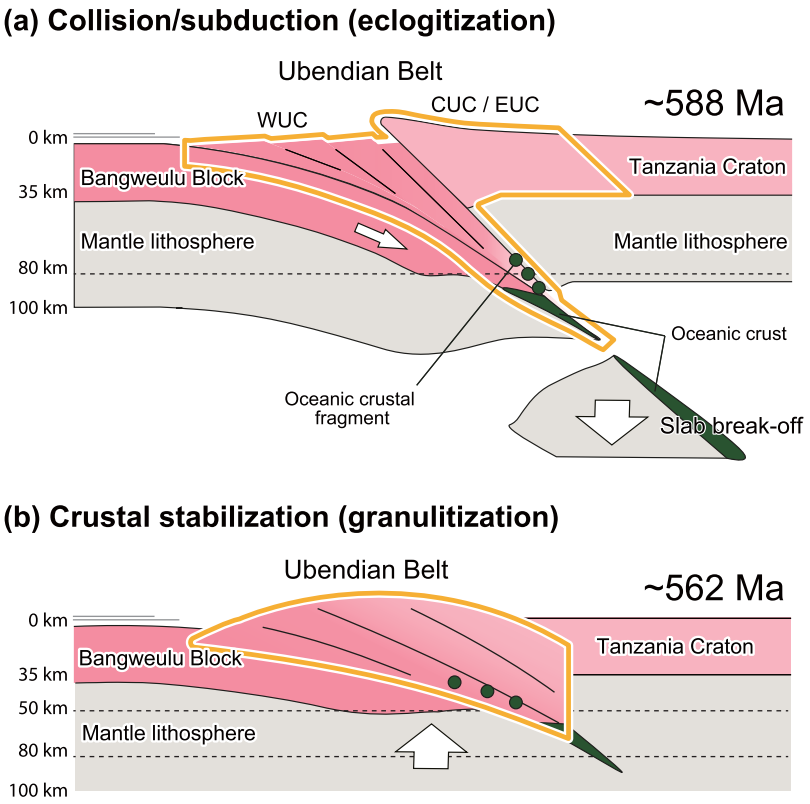

Fig. 13. A schematic cartoon illustrating the Bangweulu Craton as a microcontinent in the Neoproterozoic era collide with the Tanzania Craton and the continental crust thickened. (a) Timing of collision/subduction (eclogitization) at ~588 Ma, which shows that continental subduction to eclogite-facies depth followed by slab break-off and oceanic crust fragmentation. (b) Timing of lower crustal stabilization (granulitization) at ~562 Ma, which shows that subducted continental crust underplated to the hanging wall continental crust with the fragment of oceanic crust.

CONCLUSIONS

Petrological and geochemical studies of the basaltic bimineralic eclogite and gabbro-dioritic granulitized kyanite eclogite define three metamorphic stages in the Ufipa Terrane of Tanzania: eclogite-facies metamorphism (M1), H*P* granulite-facies overprinting (M2), and amphibolite-facies retrogression (M3). A nearly isothermal decompressive exhumation path characterizes the transition from the M1 stage at 2.1–2.6 GPa and 650–860°C to the M2 stage at 1.4–1.6 GPa and 750–940°C. Zirconology revealed the eclogite-to granulite transition time (Δt) of ~26 ± 3 Myr between 588 ± 3 and 562 ± 3 Ma, giving then an average rate of the eclogite exhumation toward lower crustal levels of 0.7–1.5 mm/year. In the exhumation process of the Ufipa Terrane, lower density gabbro-dioritic eclogite, and host felsic rocks play an essential role in carrying high-density basaltic eclogite.

The Δt value of the Ufipa Terrane is also in agreement with other large-type collisional orogens, suggesting that stabilization of thickened continental crust followed by a single continental collision event requires 20–30 Myr. This relatively long exhuming duration is also consistent with the lower-angle subduction model simulation on our thermomechanical modeling.

FUNDING

This work was supported by CNEAS, Tohoku University, and the Okayama University of Science in part by grants from the JSPS KAKENHI (JP21H01174, JP18H01299, JP15H05212, and JP24403010) to T.T. This was also supported by the MEXT Private University Research Branding Project (Okayama University of Science) to K.A. and KAKENHI JP19K04043 to K.A.

DATA AVAILABILITY STATEMENT

The data underlying this article are available in the article and in its online supplementary material.

SUPPLEMENTARY DATA

Supplementary data are available at *Journal of Petrology* online.

ACKNOWLEDGEMENT

We are grateful for constructive comments from Bernard Bingen and anonymous reviewers, and thoughtful editorial handing by Sarah Sherlock. We would like to thank Tan Furukawa for his support of numerical approaches. We thank Shota Matsunaga, Hironobu Harada and Ryo Fukushima for their laboratory assistance. We are also grateful for constructive feedback from Daniel Pastor-Gálan and Ariuntsetseg Ganbat. TT and NB thank R. Kinyaiya for driving us safely in a Toyota Land Cruiser 70 in difficult but beautiful field conditions.

REFERENCES

Aoki, S., Aoki, K., Tsuchiya, Y. & Kato, D. (2019). Constraint on the eclogite age of the Sanbagawa metamorphic rocks in Central Shikoku, Japan. *International Geology Review* **61**, 2211–2226.

Aoki, S., Aoki, K., Tsujimori, T., Sakata, S. & Tsuchiya, Y. (2020). Oceanic-arc subduction, stagnation, and exhumation: zircon U–Pb geochronology and trace-element geochemistry of the Sanbagawa eclogites in Central Shikoku SW Japan. *Lithos* **358-359**, 105378.

Baldwin, S. L., Monteleone, B. D., Webb, L. E., Fitzgerald, P. G., Grove, M. & Hill, E. J. (2004). Pliocene eclogite exhumation at plate tectonic rates in eastern Papua New Guinea. *Nature* **431**, 263–267.

Baldwin, J. A., Powell, R., White, R. W. & Štípská, P. (2015). Using calculated chemical potential relationships to account for replacement of kyanite by symplectite in high pressure granulites. *Journal of Metamorphic Geology* **33**, 311–330.

Banno, S., Enami, M., Hirajima, T., Ishiwatari, A. & Wang, Q. C. (2000). Decompression P–T path of coesite eclogite to granulite from Weihai, eastern China. *Lithos* **52**, 97–108.

Begg, G. C., Griffin, W. L., Natapov, L. M., O'Reilly, S. Y., Grand, S. P., O'Neill, C. J., Hronsky, J. M. A., Djomani, Y. P., Swain, C. J., Deen, T. & Bowden, P. (2009). The lithospheric architecture of Africa: seismic tomography, mantle petrology, and tectonic evolution. *Geosphere* **5**, 23–50.

Bingen, B., Jacobs, J., Viola, G., Henderson, I. H. C., Skår, Ø., Boyd, R. & Daudi, E. X. F. (2009). Geochronology of the Precambrian crust in the Mozambique belt in NE Mozambique, and implications for Gondwana assembly. *Precambrian Research* **170**, 231–255.

Bittner, D. & Schmeling, H. (1995). Numerical modeling of melting processes and induced diapirism in the lower crust. *Geophysical Journal International* **123**, 59–70.

Boniface, N. & Appel, P. (2018). Neoproterozoic reworking of the Ubendian Belt crust: implication for an orogenic cycle between the Tanzania Craton and Bangweulu Block during the assembly of Gondwana. *Precambrian Research* **305**, 358–385.

Boniface, N. & Schenk, V. (2012). Neoproterozoic eclogites in the Paleoproterozoic Ubendian belt of Tanzania: evidence for a Pan-African suture between the Bangweulu Block and the Tanzania Craton. *Precambrian Research* **208–211**, 72–89.

Boniface, N., Schenk, V. & Appel, P. (2014). Mesoproterozoic high-grade metamorphism in pelitic rocks of the northwestern Ubendian Belt: implication for the extension of the Kibaran intra-continental basins to Tanzania. *Precambrian Research* **249**, 215–228.

Boniface, N. & Tsujimori, T. (2019). Pillow lava basalts with back–arc MORB affinity from the Usagaran Belt, Tanzania: relics of Orosirian ophiolites. *Journal of the Geological Society* **176**, 1007–1021.

Boniface, N. & Tsujimori, T. (2021). New tectonic model and division of the Ubendian–Usagaran Belt, Tanzania: a review and in-situ dating of eclogites. *Geological Society of America Special Paper* **552**, 133–175.

Brown, M. & Johnson, T. (2018). Secular change in metamorphism and the onset of global plate tectonics. *American Mineralogist* **103**, 181–196.

Burg, J. P. & Gerya, T. V. (2005). The role of viscous heating in Barrovian metamorphism of collisional orogens: thermomechanical models and application to the Lepontine Dome in the Central Alps. *Journal of Metamorphic Geology* **23**, 75–95.

Burov, E., François, T., Agard, P., Le Pourhiet, L., Meyer, B., Tirel, C., Lebedev, S., Yamato, P. & Brun, J. P. (2014). Rheological and geodynamic controls on the mechanisms of subduction and HP/UHP exhumation of crustal rocks during continental collision: insights from numerical models. *Tectonophysics* **631**, 212–250.

Butler, J. P., Jamieson, R. A., Dunning, G. R., Pecha, M. E., Robinson, P. & Steenkamp, H. M. (2018). Timing of metamorphism and exhumation in the Nordøyane ultra-high-pressure domain, Western Gneiss Region, Norway: new constraints from complementary CA-ID-TIMS and LA-MC-ICP-MS geochronology. *Lithos* **310–311**, 153–170.

Cao, W., Gilotti, J. A., Massonne, H. J., Ferrando, S. & Foster, C. T., Jr. (2019). Partial melting due to breakdown of an epidote-group mineral during exhumation of ultrahigh-pressure eclogite: an example from the north-East Greenland Caledonides. *Journal of Metamorphic Geology* **37**, 15–39.

de Capitani, C. & Brown, T. H. (1987). The computation of chemical equilibrium in complex systems containing non-ideal solutions. *Geochimica et Cosmochimica Acta* **51**, 2639–2652.

de Capitani, C. & Petrakakis, K. (2010). The computation of equilibrium assemblage diagrams with Theriak/Domino software. *American Mineralogist* **95**, 1006–1016.

Carswell, D. A. & O'Brien, P. J. (1993). Thermobarometry and geotectonic significance of high-pressure granulites: examples from the Moldanubian Zone of the Bohemian Massif in Lower Austria. *Journal of Petrology* **34**, 427–459.

Chemenda, A. I., Burg, J. P. & Mattauer, M. (2000). Evolutionary model of the Himalaya–Tibet system: geopoem: based on new modeling, geological and geophysical data. *Earth and Planetary Science Letters* **174**, 397–409.

Chen, Y., Xu, Y., Xu, T., Si, S., Liang, X., Tian, X., Deng, Y., Chen, L., Wang, P., Xu, Y., Lan, H., Xiao, F., Li, W., Zhang, X., Yuan, X., Badal, J. & Teng, J. (2015). Magmatic underplating and crustal growth in the Emeishan Large Igneous Province, SW China, revealed by a passive seismic experiment. *Earth and Planetary Science Letters* **432**, 103–114.

Chung, S. L., Chu, M. F., Ji, J., O'Reilly, S. Y., Pearson, N. J., Liu, D., Lee, T. H. & Lo, C. H. (2009). The nature and timing of crustal thickening in Southern Tibet: geochemical and zircon Hf isotopic constraints from postcollisional adakites. *Tectonophysics* **477**, 36–48.

Clauser, C. & Huenges, E. (1995). Thermal conductivity of rocks and minerals. *Rock Physics & Phase Relations: A Handbook of Physical Constants* **3**, 105–126.

Cutten, H., Johnson, S. P. & Waele, B. D. (2006). Protolith ages and timing of metasomatism related to the formation of whiteschists at Mautia Hill, Tanzania: implications for the assembly of Gondwana. *The Journal of Geology* **114**, 683–698.

Daly, M. C. (1988). Crustal shear zones in Central Africa: a kinematic approach to Proterozoic tectonics. *Episodes* **11**, 5–11.

Dziewonski, A. M. & Anderson, D. L. (1981). Preliminary reference earth model. *Physics of the Earth and Planetary Interiors* **25**, 297–356.

Ellis, D. J. & Green, D. H. (1979). An experimental study of the effect of Ca upon garnet-clinopyroxene Fe-Mg exchange equilibria. *Contributions to Mineralogy and Petrology* **71**, 13–22.

Ernst, W. G., Maruyama, S. & Wallis, S. (1997). Buoyancy-driven, rapid exhumation of ultrahigh-pressure metamorphosed continental crust. *Proceedings of the National Academy of Sciences* **94**, 9532–9537.

Faryad, S. W., Nahodilová, R. & Dolejš, D. (2010). Incipient eclogite facies metamorphism in the Moldanubian granulites revealed by mineral inclusions in garnet. *Lithos* **114**, 54–69.

Flores, K. E., Martens, U. C., Harlow, G. E., Brueckner, H. K. & Pearson, N. J. (2013). Jadeitite formed during subduction: in situ zircon geochronology constraints from two different tectonic events within the Guatemala Suture Zone. *Earth and Planetary Science Letters* **371**, 67–81.

Fritz, H., Tenczer, V., Hauzenberger, C. A., Wallbrecher, E., Hoinkes, G., Muhongo, S. & Mogessie, A. (2005). Central Tanzanian tectonic map: a step forward to decipher Proterozoic structural events in the East African Orogen. *Tectonics* **24**, TC6013.

Fritz, H., Tenczer, V., Hauzenberger, C., Wallbrecher, E. & Muhongo, S. (2009). Hot granulite nappes—tectonic styles and thermal evolution of the Proterozoic granulite belts in East Africa. *Tectonophysics* **477**, 160–173.

Fritz, H., Abdelsalam, M., Ali, K. A., Bingen, B., Collins, A. S., Fowler, A. R., Ghebread, W., Hauzenberger, C. A., Johnson, P. R., Kusky, T. M., Macey, P., Muhougo, S., Stern, R. J. & Viola, G. (2013). Orogen styles in the East African Orogen: a review of the Neoproterozoic to Cambrian tectonic evolution. *Journal of African Earth Sciences* **86**, 65–106.

Frost, C. D., Bell, J. M., Frost, B. R. & Chamberlain, K. R. (2001). Crustal growth by magmatic underplating: isotopic evidence from the northern Sherman batholith. *Geology* **29**, 515–518.

Ganbat, A., Tsujimori, T., Boniface, N., Pastor-Galán, D., Aoki, S. & Aoki, K. (2021). Crustal evolution of the Paleoproterozoic Ubendian Belt (SW Tanzania) western margin: a Central African Shield amalgamation tale. *Gondwana Research* **91**, 286–306.

Gerya, T. V. (2009) *Introduction to Numerical Geodynamic Modelling*. Cambridge University Press.

Gerya, T. V. & Yuen, D. A. (2003). Characteristics-based marker-in-cell method with conservative finite-differences schemes for modeling geological flows with strongly variable transport properties. *Physics of the Earth and Planetary Interiors* **140**, 293–318.

Gerya, T. V., Connolly, J. A., Yuen, D. A., Gorczyk, W. & Capel, A. M. (2006). Seismic implications of mantle wedge plumes. *Physics of the Earth and Planetary Interiors* **156**, 59–74.

Grantham, G. H., Maboko, M. & Eglington, B. M. (2003). A review of the evolution of the Mozambique Belt and implications for the amalgamation and dispersal of Rodinia and Gondwana. *Geological Society, London, Special Publications* **206**, 401–425.

Hacker, B. R., Kylander-Clark, A. R., Holder, R., Andersen, T. B., Peterman, E. M., Walsh, E. O. & Munnikhuis, J. K. (2015). Monazite response to ultrahigh-pressure subduction from U–Pb dating by laser ablation split stream. *Chemical Geology* **409**, 28–41.

Harlow, G. E. (1998). Interpretation of KCpx and CaEs in clinopyroxene from diamond inclusions and mantle samples. In: *International Kimberlite Conference: Extended Abstracts*, vol. **7**, pp. 299–301.

Hermann, J., Rubatto, D., Korsakov, A. & Shatsky, V. S. (2001). Multiple zircon growth during fast exhumation of diamondiferous, deeply subducted continental crust (Kokchetav Massif, Kazakhstan). *Contributions to Mineralogy and Petrology* **141**, 66–82.

Hess, P. C. (1989) *Origin of Igneous Rocks*. Harvard University Press.

Hirschmann, M. M. (2000). Mantle solidus: experimental constraints and the effects of peridotite composition. *Geochemistry, Geophysics, Geosystems* **1**, 2000GC000070.

Hofmeister, A. M. (1999). Mantle values of thermal conductivity and the geotherm from phonon lifetimes. *Science* **283**, 1699–1706.

Holland, T. & Blundy, J. (1994). Non-ideal interactions in calcic amphiboles and their bearing on amphibole-plagioclase thermometry. *Contributions to Mineralogy and Petrology* **116**, 433–447.

Holland, T. J. B. & Powell, R. (1998). An internally consistent thermodynamic data set for phases of petrological interest. *Journal of Metamorphic Geology* **16**, 309–343.

Houseman, G. & England, P. (1993). Crustal thickening versus lateral expulsion in the Indian–Asian continental collision. *Journal of Geophysical Research: Solid Earth* **98**, 12233–12249.

Itano, K., Iizuka, T., Chang, Q., Kimura, J. I. & Maruyama, S. (2016). U–Pb chronology and geochemistry of detrital monazites from major African rivers: constraints on the timing and nature of the Pan-African Orogeny. *Precambrian Research* **282**, 139–156.

Jochum, K. P., Weis, U., Stoll, B., Kuzmin, D., Yang, Q., Raczek, I., Jacob, D., Stracke, A., Birbaum, K., Frick, D., Gü nther, D. & Enzweiler, J. (2011). Determination of reference values for NIST SRM 610–617 glasses following ISO guidelines. *Geostandards and Geoanalytical Research* **35**, 397–429.

Johannes, W. (1985). The significance of experimental studies for the formation of migmatites. In: *Migmatites*, pp. 36–85. Boston, MA, USA: Springer.

John, T., Schenk, V., Haase, K., Scherer, E. & Tembo, F. (2003). Evidence for a Neoproterozoic ocean in south-central Africa from mid-oceanic-ridge–type geochemical signatures and pressure-temperature estimates of Zambian eclogites. *Geology* **31**, 243–246.

Johnson, S. P., Cutten, H. N. C., Muhongo, S. & De Waele, B. (2003). Neoarchaean magmatism and metamorphism of the western granulites in the central domain of the Mozambique belt, Tanzania: U–Pb shrimp geochronology and PT estimates. *Tectonophysics* **375**, 125–145.

Kellett, D. A., Cottle, J. M. & Smit, M. (2014). Eocene deep crust at Ama Drime, Tibet: early evolution of the Himalayan orogen. *Lithosphere* **6**, 220–229.

Kröner, A. (1984). Done structures and basement reactivation in the Pan-African Damara belt of Namibia. In: *Precambrian Tectonics Illustrated*, pp. 191–206.

Kröner, A. & Stern, R. J. (2004). Pan-African Orogeny. *Encyclopedia* of *Geology* **1**, 1–12.

Kröner, A., Eyal, M. & Eyal, Y. (1990). Early Pan-African evolution of the basement around Elat, Israel, and the Sinai Peninsula revealed by single-zircon evaporation dating, and implications for crustal accretion rates. *Geology* **18**, 545–548.

Kusky, T. M., Abdel Salam, M. G., Stern, R. J. & Tucker, R. D. (2003). Evolution of the East African and related orogens, and the assembly of Gondwana. *Precambrian Research* **123**, 81–85.

Kylander-Clark, A. R., Hacker, B. R. & Mattinson, C. G. (2012). Size and exhumation rate of ultrahigh-pressure terranes linked to orogenic stage. *Earth and Planetary Science Letters* **321-322**, 115–120.

Lenoir, J. L., Liégeois, J. P., Theunissen, K. & Klerkx, J. (1994). The Palaeoproterozoic Ubendian shear belt in Tanzania: geochronology and structure. *Journal of African Earth Sciences* **19**, 169–184.

Li, Z. (2014). A review on the numerical geodynamic modeling of continental subduction, collision and exhumation. *Science China Earth Sciences* **57**, 47–69.

Li, Z. H., Xu, Z. Q. & Gerya, T. V. (2011). Flat versus steep subduction: contrasting modes for the formation and exhumation of high-to ultrahigh-pressure rocks in continental collision zones. *Earth and Planetary Science Letters* **301**, 65–77.

Liao, X., Liu, L., Wang, Y., Cao, Y., Chen, D. & Dong, Y. (2016). Multi-stage metamorphic evolution of retrograde eclogite with a granulite-facies overprint in the Zhaigen area of the North Qinling Belt, China. *Gondwana Research* **30**, 79–96.

Liou, J. G., Ernst, W. G., Zhang, R. Y., Tsujimori, T. & Jahn, B. M. (2009). Ultrahigh-pressure minerals and metamorphic terranes—the view from China. *Journal of Asian Earth Sciences* **35**, 199–231.

Liou, J. G., Tsujimori, T., Yang, J., Zhang, R. Y. & Ernst, W. G. (2014). Recycling of crustal materials through study of ultrahigh-pressure minerals in collisional orogens, ophiolites, and mantle xenoliths: a review. *Journal of Asian Earth Sciences* **96**, 386–420.

Liu, F. L. & Liou, J. G. (2011). Zircon as the best mineral for P–T–time history of UHP metamorphism: a review on mineral inclusions and U–Pb SHRIMP ages of zircons from the Dabie–Sulu UHP rocks. *Journal of Asian Earth Sciences* **40**, 1–39.

Liu, Y., Zong, K., Kelemen, P. B. & Gao, S. (2008). Geochemistry and magmatic history of eclogites and ultramafic rocks from the Chinese continental scientific drill hole: subduction and ultrahigh-pressure metamorphism of lower crustal cumulates. *Chemical Geology* **247**, 133–153.

Ma, C., Li, Z., Ehlers, C., Yang, K. & Wang, R. (1998). A post-collisional magmatic plumbing system: Mesozoic granitoid plutons from the Dabieshan high-pressure and ultrahigh-pressure metamorphic zone, east-central China. *Lithos* **45**, 431–456.

Maboko, M. A. & Nakamura, E. (1996). Nd and Sr isotopic mapping of the Archaean-Proterozoic boundary in southeastern Tanzania using granites as probes for crustal growth. *Precambrian Research* **77**, 105–115.

Mattinson, C. G., Wooden, J. L., Liou, J. G., Bird, D. K. & Wu, C. L. (2006). Age and duration of eclogite-facies metamorphism, North Qaidam HP/UHP terrane, Western China. *American Journal of Science* **306**, 683–711.

McDonough, W. F. & Sun, S. S. (1995). The composition of the Earth. *Chemical Geology* **120**, 223–253.

Meert, J. G. (2003). A synopsis of events related to the assembly of eastern Gondwana. *Tectonophysics* **362**, 1–40.

Meert, J. G. & Lieberman, B. S. (2008). The Neoproterozoic assembly of Gondwana and its relationship to the Ediacaran–Cambrian radiation. *Gondwana Research* **14**, 5–21.

Mo, X., Hou, Z., Niu, Y., Dong, G., Qu, X., Zhao, Z. & Yang, Z. (2007). Mantle contributions to crustal thickening during continental collision: evidence from Cenozoic igneous rocks in southern Tibet. *Lithos* **96**, 225–242.

Molina, J. F., Moreno, J. A., Castro, A., Rodríguez, C. & Fershtater, G. B. (2015). Calcic amphibole thermobarometry in metamorphic and igneous rocks: new calibrations based on plagioclase/amphibole Al-Si partitioning and amphibole/liquid mg partitioning. *Lithos* **232**, 286–305.

Mori, K., Tsujimori, T. & Boniface, N. (2018). Finding of talc–and kyanite–bearing amphibolite from the Paleoproterozoic Usagaran Belt, Tanzania. *Journal of Mineralogical and Petrological Sciences* **113**, 316–321.

Mruma, A. H. (1989) *Stratigraphy, Metamorphism and Tectonic Evolution of the Early Proterozoic Usagaran Belt*. Research Terrae (Series A): Tanzania, p.193.

Nakamura, D. (2009). A new formulation of garnet–clinopyroxene geothermometer based on accumulation and statistical analysis of a large experimental data set. *Journal of Metamorphic Geology* **27**, 495–508.

Nakamura, D. & Banno, S. (1997). Thermodynamic modeling of sodic pyroxene solid-solution and its application in a garnet-omphacite-kyanite-coesite geothermobarometer for UHP metamorphic rocks. *Contributions to Mineralogy and Petrology* **130**, 93–102.

Nance, R. D. & Murphy, J. B. (2019). Supercontinents and the case for Pannotia. *Geological Society, London, Special Publications* **470**, 65–86.

Palin, R. M., Weller, O. M., Waters, D. J. & Dyck, B. (2016). Quantifying geological uncertainty in metamorphic phase equilibria modeling; a Monte Carlo assessment and implications for tectonic interpretations. *Geoscience Frontiers* **7**, 591–607.

Palin, R. M., Santosh, M., Cao, W., Li, S. S., Hernández-Uribe, D. & Parsons, A. (2020). Secular change and the onset of plate tectonics on Earth. *Earth-Science Reviews* **207**, 103172.

Poli, S. & Schmidt, M. W. (2002). Petrology of subducted slabs. *Annual Review of Earth and Planetary Sciences* **30**, 207–235.

Powell, R. (1985). Regression diagnostics and robust regression in geothermometer/geobarometer calibration: the garnet-clinopyroxene geothermometer revisited. *Journal of Metamorphic Geology* **3**, 231–243.

Powell, R. & Holland, T. J. B. (2008). On thermobarometry. *Journal of Metamorphic Geology* **26**, 155–179.

Ranalli, G. (1995) *Rheology of the Earth*. Springer Science & Business Media.

Ravna, K. (2000). The garnet–clinopyroxene Fe^{2+}–Mg geothermometer: an updated calibration. *Journal of Metamorphic Geology* **18**, 211–219.

Reddy, S. M., Collins, A. S. & Mruma, A. (2003). Complex high-strain deformation in the Usagaran Orogen, Tanzania: structural setting of Palaeoproterozoic eclogites. *Tectonophysics* **375**, 101–123.

Ring, U., Kröner, A., Buchwaldt, R., Toulkeridis, T. & Layer, P. W. (2002). Shear-zone patterns and eclogite-facies metamorphism in the Mozambique belt of northern Malawi, east-central Africa: implications for the assembly of Gondwana. *Precambrian Research* **116**, 19–56.

Rino, S., Kon, Y., Sato, W., Maruyama, S., Santosh, M. & Zhao, D. (2008). The Grenvillian and Pan-African orogens: world's largest orogenies through geologic time, and their implications on the origin of superplume. *Gondwana Research* **14**, 51–72.

Rubatto, D. (2002). Zircon trace element geochemistry: partitioning with garnet and the link between U–Pb ages and metamorphism. *Chemical Geology* **184**, 123–138.

Rubatto, D. & Hermann, J. (2001). Exhumation as fast as subduction? *Geology* **29**, 3–6.

Sakata, S., Hirakawa, S., Iwano, H., Danhara, T., Guillong, M. & Hirata, T. (2017). A new approach for constraining the magnitude of initial disequilibrium in quaternary zircons by coupled uranium and thorium decay series dating. *Quaternary Geochronology* **38**, 1–12.

da Silva, L. C., McNaughton, N. J., Armstrong, R., Hartmann, L. A. & Fletcher, I. R. (2005). The Neoproterozoic Mantiqueira Province and its African connections: a zircon-based U–Pb geochronologic subdivision for the Brasiliano/Pan-African systems of orogens. *Precambrian Research* **136**, 203–240.

Sizova, E., Gerya, T. & Brown, M. (2014). Contrasting styles of Phanerozoic and Precambrian continental collision. *Gondwana Research* **25**, 522–545.

Sláma, J., Košler, J., Condon, D. J., Crowley, J. L., Gerdes, A., Hanchar, J. M. & Whitehouse, M. J. (2008). Plešovice zircon—a new natural reference material for U–Pb and Hf isotopic microanalysis. *Chemical Geology* **249**, 1–35.

Song, S., Zhang, L., Niu, Y., Su, L., Song, B. & Liu, D. (2006). Evolution from oceanic subduction to continental collision: a case study from the Northern Tibetan Plateau based on geochemical and geochronological data. *Journal of Petrology* **47**, 435–455.

Stern, R. J. (1994). Arc assembly and continental collision in the Neoproterozoic East African Orogen: implications for the consolidation of Gondwanaland. *Annual Review of Earth and Planetary Sciences* **22**, 319–351.

Stern, R. A. (1997). The GSC sensitive high resolution ion microprobe (SHRIMP): analytical techniques of zircon U-Th-Pb age determinations and performance evaluation. *Radiogenic Age and Isotopic Studies: Report* **10**, 1–31.

Stern, R. J. & Kröner, A. (1993). Late Precambrian crustal evolution in NE Sudan: isotopic and geochronologic constraints. *The Journal of Geology* **101**, 555–574.

Štípská, P., Powell, R., Hacker, B. R., Holder, R. & Kylander-Clark, A. R. C. (2016). Uncoupled U/Pb and REE response in zircon during the transformation of eclogite to mafic and intermediate granulite (Blanský les, Bohemian Massif). *Journal of Metamorphic Geology* **34**, 551–572.

Sun, S. S. & McDonough, W. F. (1989). Chemical and isotopic systematics of oceanic basalts: implications for mantle composition and processes. *Geological Society, London, Special Publications* **42**, 313–345.

Tamblyn, R., Brown, D., Hand, M., Morrissey, L., Clark, C. & Anczkiewicz, R. (2020). The 2 Ga eclogites of Central Tanzania: directly linking age and metamorphism. *Lithos* **105890**.

Tenczer, V., Hauzenberger, C. A., Fritz, H., Whitehouse, M. J., Mogessie, A., Wallbrecher, E. & Hoinkes, G. (2006). Anorthosites in the Eastern Granulites of Tanzania–new SIMS zircon U–Pb age data, petrography and geochemistry. *Precambrian Research* **148**, 85–114.

Thybo, H. & Artemieva, I. M. (2013). Moho and magmatic underplating in continental lithosphere. *Tectonophysics* **609**, 605–619.

Torsvik, T. H. & Cocks, L. R. M. (2013). Gondwana from top to base in space and time. *Gondwana Research* **24**, 999–1030.

Tsujimori, T. & Ernst, W. G. (2014). Lawsonite blueschists and lawsonite eclogites as proxies for palaeo-subduction zone processes: a review. *Journal of Metamorphic Geology* **32**, 437–454.

Tsujimori, T. & Mattinson, C. (2021) Eclogites in different tectonic settings. In: (Elias S. & Alderton D. (eds)) *Encyclopedia of Geology*, 2nd edn. Academic Press, pp.561–568.

Turcotte, D. L. & Schubert, G. (2018) *Geodynamics*.

Veevers, J. J. (2003). Pan-African is pan-Gondwanaland: oblique convergence drives rotation during 650–500 Ma assembly. *Geology* **31**, 501–504.

Vermeesch, P. (2018). IsoplotR: a free and open toolbox for geochronology. *Geoscience Frontiers* **9**, 1479–1493.

Viola, G., Henderson, I. H. C., Bingen, B., Thomas, R. J., Smethurst, M. D. & De Azavedo, S. (2008). Growth and collapse of a deeply eroded orogen: insights from structural, geophysical, and geochronological constraints on the Pan-African evolution of NE Mozambique. *Tectonics*(5) **27**.

Walsh, E. O. & Hacker, B. R. (2004). The fate of subducted continental margins: two-stage exhumation of the high-pressure to ultrahigh-pressure Western Gneiss Region, Norway. *Journal of Metamorphic Geology* **22**, 671–687.

Wang, Y., Zhang, L. F., Li, Z. H., Li, Q. Y. & Bader, T. (2019). The exhumation of subducted oceanic-derived eclogites: insights from phase equilibrium and thermomechanical modeling. *Tectonics* **38**, 1764–1797.

Warren, C. J., Beaumont, C. & Jamieson, R. A. (2008). Deep subduction and rapid exhumation: role of crustal strength and strain weakening in continental subduction and ultrahigh-pressure rock exhumation. *Tectonics* **27**.

Whitney, D. L. & Evans, B. W. (2010). Abbreviations for names of rock-forming minerals. *American Mineralogist* **95**, 185–187.

Wiedenbeck, M. A. P. C., Alle, P., Corfu, F., Griffin, W. L., Meier, M., Oberli, F. V. & Spiegel, W. (1995). Three natural zircon standards for U-Th-Pb, Lu-Hf, trace element and REE analyses. *Geostandards Newsletter* **19**, 1–23.

Wiedenbeck, M., Hanchar, J. M., Peck, W. H., Sylvester, P., Valley, J., Whitehouse, M. & Zheng, Y. F. (2004). Further characterisation of the 91500 zircon crystal. *Geostandards and Geoanalytical Research* **28**, 9–39.

de Wit, M. J., & Linol, B. (2015). Precambrian basement of the Congo Basin and its flanking terrains. In: *Geology and Resource Potential of the Congo Basin*, pp. 19–37. Berlin, Heidelberg: Springer.

Yakymchuk, C., Kirkland, C. L. & Clark, C. (2018). Th/U ratios in metamorphic zircon. *Journal of Metamorphic Geology* **36**, 715–737.